

# Analytical design criteria for realizing ideal standard filters in strongly coupled resonant systems, with application to microwave metasurfaces

Mohammed Benzaouia <sup>1,\*</sup>, John D. Joannopoulos,<sup>2</sup> Steven G. Johnson <sup>3</sup> and Aristeidis Karalis <sup>4,†</sup>

<sup>1</sup>*Department of Electrical Engineering and Computer Science,  
Massachusetts Institute of Technology, Cambridge, MA 02139, USA.*

<sup>2</sup>*Department of Physics, Massachusetts Institute of Technology, Cambridge, MA 02139, USA.*

<sup>3</sup>*Department of Mathematics, Massachusetts Institute of Technology, Cambridge, MA 02139, USA.*

<sup>4</sup>*Research Laboratory of Electronics, Massachusetts Institute of Technology, Cambridge, MA 02139, USA.*

We present general analytical criteria for the precise design of symmetric or “antimetric” 2-port systems, including ideal standard filters (Chebyshev, elliptic, etc.), based on the non-normalized resonant (quasi-normal) modes of the system. We first develop a quasi-normal mode theory (QNMT) to calculate a system’s scattering  $S$  matrix, satisfying both energy conservation and reciprocity, and describe how low- $Q$  modes can be combined into an effective slowly varying background response  $C$ . We then show that the resonant QNM fields of *all* lossless reciprocal 2-port systems with a symmetric ( $S_{22} = S_{11}$ ) or “antimetric” ( $S_{22} = -S_{11}$ ) response couple to the input and output ports with specific unitary ratios, whose relative signs determine the position of the scattering zeros. This allows us to obtain design criteria assigning values to the poles, background response, and QNM-to-ports coupling coefficients. Filter devices can then be designed via a well-conditioned nonlinear optimization (or root-finding) problem using a numerical eigensolver. As an example application, we design microwave metasurface filters that precisely match standard amplitude filters of various orders and bandwidths, with focus on the best-performing elliptic filters.

## I. INTRODUCTION

High-order (multi-resonance) filters—especially ideal standard filters (ISFs), such as Butterworth or elliptic [1]—have been designed for many types of wave physics (electromagnetic [2–12], mechanical [13–17], etc.) by a variety of techniques, including brute-force optimization of the transmission/scattering spectrum [18–21], circuit theory in the microwave regime [22–31], and coupled-mode theory (CMT) [32–34] for cascaded optical resonators [2–8]. Circuit theory and CMT provide attractive semi-analytical frameworks for filter design, but are restricted to systems composed of spatially separable components (either discrete circuit elements or weakly coupled resonances, respectively), while brute-force spectrum optimization faces several numerical challenges. To design ultra-compact filters, involving strongly coupled elements and spatially overlapping resonances, a precise, systematic and computationally tractable methodology is missing. In this article, we develop a new such filter-design approach by deriving a minimal set of explicit *analytical* criteria on the system resonances, applicable to all symmetric and “antimetric” [35] filters, including ISFs. To derive these conditions, we first improve the quasi-normal-mode (QNM) expansion of the scattering matrix  $S$  [36] to ensure that  $S$  simultaneously satisfies all physical constraints of time-domain realness, energy conservation, and reciprocity, in contrast to previous QNM theory (QNMT) formulations [36, 37], and we further show how low- $Q$  resonances can be folded into a separate background scattering term  $C$ . We then use our  $S$

expansion to derive the required coupling coefficients of the resonances (QNMs) to the input and output ports in conjunction with the net background response, in order to achieve multiple configurations for the zeros of the  $S$  coefficients (generalizing previous work [38, 39]) and thus realize any desired ISF. We finally apply our procedure to computationally design microwave metasurface filters that precisely match ISFs of various orders, bandwidths, and types—especially optimal elliptic filters, which were demonstrated only approximately in the past [21–25].

The resonant modes of open physical systems, often called “quasi-normal modes” (QNM) as they are not square-integrable and exponentially diverge outside the resonator, can allow a fast approximate solution and a good physical interpretation of scattering and emission problems [40–42]. However, their far-field divergence has led to many challenges, most of which can be addressed via appropriate normalizations at the price of increased complexity [43]. A new phenomenological approach was proposed in Ref. 36, starting from the CMT equations, to obtain a QNM expansion of  $S$  with good accuracy without the need to normalize the modes. However, for lossless reciprocal systems, that formulation does not guarantee energy conservation. This is an essential physical requirement, so we show in Sec. II that the QNM-to-ports coupling coefficients can be fine-tuned to simultaneously enforce realness, energy conservation and reciprocity of  $S$ . We demonstrate this method for both 2-port and 4-port examples using metasurfaces, and with excitation of both normally and obliquely incident plane waves, the latter requiring evaluation of unusual eigenmodes with complex Bloch wavevectors. Moreover, we extend our QNMT to cases of non-trivial direct-scattering pathways with a slowly-varying background response  $C$ , by separating low- from high- $Q$  modes in a way that provides

\* Corresponding author: medbenz@mit.edu

† Corresponding author: aristos@mit.edu

an additional approximate formula  $S = \bar{S}C$ , which we show to be very useful for filter design, because it greatly reduces the complexity of the model.

Topology-optimization design (including widely used inverse-adjoint methods and machine-learning algorithms) is a powerful approach to design complex structures by optimizing thousands of degrees of freedom [44]. However, if the optimization problem is formulated directly in terms of matching a desired transmission spectrum, it can face severe numerical challenges: the highly oscillatory nature of the transmission spectrum can trap optimizers in poor local optima, and stringent constraints (e.g. on stop- and pass-band transmission) can lead to very “stiff” optimization problems with slow convergence. (A proposed solution was to restrict the designs to spatially distinct resonators as in CMT [45].) However, when analytical solutions to *parts* of the problem exist, the numerical side of the optimization can be rendered simpler and more robust. For filter design in particular, signal-processing theory analytically defines many such “optimal” filters (ISFs), characterized by various rational transfer functions with specified poles and zeros, the latter necessary to achieve a steep transition between the “pass” and “stop” frequency bands. Therefore, when designing physical filters, it is advantageous to exploit these analytical solutions. An exact methodology, called network synthesis, was developed to implement these ISFs in the extreme quasi-static (subwavelength) limit, where structures can be modeled precisely by networks of discrete elements, as in electronic circuits [1]. In the other limit of structures spanning multiple wavelengths, the direct relation between transfer-function poles and the eigenfrequencies of the physical system’s resonant modes has made temporal coupled-mode theory (CMT) [32–34] a popular design tool, especially for (high-order) optical add-drop filters [2–7], most of which are only Chebyshev or Butterworth filters with no transmission-zeros, using a symmetric topology. However, in the intermediate limit of physical structures with size on the order of the wavelength or only a few times smaller (metamaterials), no complete filter-design methodology exists. Discrete-element equivalent networks must often become overly complicated to model the full wave physics accurately and they change for each different structural topology [29] or, worse, they fail to provide any adequate model (as is typically the case in dielectric photonic structures). Therefore, network synthesis may be useful for the intuitive choice of an appropriate system topology but not for the calculation of its exact parameters. CMT, on the other hand, is typically based on weakly coupled resonators and the knowledge of the “uncoupled” modes of the system [34], but neither of these conditions usually hold for wavelength-scale structures with multiple strongly inter-coupled/overlapping resonances [46]. Still missing has been a unified, physics-independent, set of exact conditions for the precise design of filters with multiple zeros that can be fed as a smooth objective to optimization algorithms. Using our QNMT formulation,

in Sec. III we derive such simple and general rules to design ISFs using eigenmode solvers. In particular, we show that the resonant QNM fields of *all* lossless reciprocal 2-port systems with symmetric ( $S_{22} = S_{11}$ ) or “antimetric” ( $S_{22} = -S_{11}$ ) [35] response couple to the input and output ports with specific unitary ratios, whose relative signs determine the position of the scattering zeros. Thus, for filter design, apart from the obvious matching of system resonant frequencies to the desired filter’s complex poles, we explain that, to also obtain the desired-filter zeros, these ratios must be enforced for the critical filter resonances and the remaining QNMs must add up to a required overall background response.

In the design of microwave frequency-selective surfaces (FSS), most previous efforts have been based on effective-circuit models [26, 28–31], so their designs are not easily generalizable (as explained above) and attempts to synthesize elliptic filters have led to only approximately elliptic spectra [22–24]. In Sec. IV, we do discuss the relation between QNMT and effective-circuit models to motivate appropriate structural-topology choices for different filters and scattering-zero placements. However, following our systematic filter-design procedure, we then implement microwave metasurfaces that exhibit, for a normally incident plane wave, transmission spectra matching ISF responses of various orders, bandwidths and types. Notably, we demonstrate second- and third-order elliptic filters for both bandpass and bandstop behaviors. We show that, in some cases, even though symmetric performance is desired, structural asymmetry should be used, while conversely, in cases where the ideal performance is antimetric, we also present approximate symmetric solutions. The designed metasurfaces are compatible with fabrication by printed-circuit board technology, and also offer potential electrical tunability.

## II. QUASI-NORMAL MODE THEORY

In this section, we revisit the QNMT derivation of Ref. 36 for scattering problems, with some clarifications, improvements, and extensions. Specifically, we formulate the theory more straightforwardly using the system QNMs from the beginning (instead of starting from CMT using ambiguous uncoupled modes), remove a ports-reference-dependent phase function, and calculate coefficients entering the  $S$ -matrix expansion to *exactly* satisfy the physical requirements of realness, energy conservation, and reciprocity. The final result is a simple equation [Eq. (7)] to compute  $S$  using only the resonant frequencies  $\Omega$  and refined [via Eq. (11)] QNM-to-ports coupling coefficients  $D$ , without need for QNM-normalization. We also extend this theory to non-trivial direct-scattering pathways, by showing that a slowly-varying background response  $C$  can be calculated via the system low- $Q$  modes, and then placing the high- $Q$  modes into a different matrix  $\bar{S}$  allows us to obtain the good approximation  $S = \bar{S}C$  [Eq. (15)].

### A. QNMT derivation

*Formulation (Figure 1)*— We consider a general scattering problem of an arbitrary linear time-independent scatterer, coupled to incoming (excited) and outgoing (scattered) radiation via several physical *linear* ports. At the frequency  $\omega$  of excitation, the scatterer has a total of  $P$  “coupling port-modes” (CPM) of radiation, which can be either single propagating modes of  $P$  different physical ports or several propagating modes of fewer ports (while all other port-modes are either evanescent, or of incompatible symmetry, or their coupling is simply too small at  $\omega$ ). Let CPM  $p$  propagate with wavevector  $\mathbf{k}_p(\omega)$  and field  $\phi_p(\omega, \mathbf{r}) = \phi_p^\perp(\omega, \mathbf{r}_p^\perp) e^{ik_p r_p^\parallel}$ , separable in the propagation ( $r_p^\parallel$ ) and transverse ( $\mathbf{r}_p^\perp \perp \mathbf{k}_p$ ) coordinates. In the most common case of reciprocal lossless physical ports, the CPMs at  $\omega$  are orthogonal under the standard (conjugated) “power” inner product (a cross-sectional overlap surface integral) and can be normalized to carry unit power  $\langle \phi_p^\perp | \phi_q^\perp \rangle = \delta_{pq}$  [32]. Then, for the  $P$  pairs of incident and scattered CPM waves, if the vectors  $\mathbf{s}_+$  and  $\mathbf{s}_-$  denote respectively their amplitudes at specific reference cross-sections  $r_p^\parallel = c_p$  of their physical ports,  $|s_{\pm p}|^2$  equals the power carried by the  $\pm p$  wave,  $\mathbf{s}_\pm^\dagger \mathbf{s}_\pm$  is the net incident/scattered power, and the system scattering matrix  $S$  at these cross-sections is defined by  $\mathbf{s}_- = S \mathbf{s}_+$ .

Since the scattering system is open (coupled to radiation), its Hamiltonian  $H$  is non-Hermitian, so it supports a set of resonant modes [with resonant frequencies  $\omega_n$  and fields  $\psi_n(\mathbf{r})$  namely  $H(i\omega_n)\psi_n = i\omega_n\psi_n$ ], which are linearly independent but quasi-normal and non-orthogonal under the standard (conjugated) “energy” inner product (a volume integral). However, when the system is reciprocal,  $H$  is complex-symmetric, so its QNMs are orthogonal under the non-conjugated inner product  $\{\psi_n | \psi_l\} = 0$  for  $n \neq l$  [41, 42]. We consider  $N$  such modes, whose normalization we leave *unspecified*, and denote by the *diagonal* matrix  $\Omega$  their complex frequencies and by the vector  $\mathbf{a}$  their amplitudes upon excitation. Moreover, it is usually assumed there are also pathways other than the resonant QNMs for direct scattering of input to output CPM waves, through the background medium without the scatterer, quantified by a scattering matrix  $C$  [32, 34].

The part of the scattered field *not* due to direct pathways ( $\mathbf{s}_-^Q = \mathbf{s}_- - C\mathbf{s}_+$ ) can be written outside the scatterer as an expansion over the complete set of port modes (propagating CPMs and evanescent). QNMT makes the approximation that it can be written also within the volume  $V$  of the scatterer as a linear combination of the  $N$  QNMs (an assumption also used in CMT [34]):

$$\mathbf{F}_{\text{scat}}^Q = \begin{cases} \sum_{p=1}^P s_{-p}^Q(\omega) \phi_p^\perp(\omega, \mathbf{r}_p^\perp) e^{ik_p(r_p^\parallel - c_p)} + \text{evan.}; & \mathbf{r} \notin V \\ \sum_{n=1}^N a_n(\omega) \psi_n(\mathbf{r}); & \mathbf{r} \in V. \end{cases} \quad (1)$$

By inserting the second line into the exact equation for

the field inside the scatterer and by mode-matching the two lines on the cross-section  $c'_p$  where the  $p$ -port meets the scatterer boundary, one respectively gets the final two QNMT equations, which, with  $\exp(-i\omega t)$  notation, take the form (rigorous derivation for example in Ref. 37):

$$\begin{aligned} -i(\omega - \Omega) \mathbf{a} &= K^t \mathbf{s}_+ \\ \mathbf{s}_- - C\mathbf{s}_+ &= D\mathbf{a}, \end{aligned} \quad (2)$$

where

$$D_{pn}(\omega) = e^{ik_p l_p} \langle \phi_p^\perp(\omega, \mathbf{r}_p^\perp) | \psi_n(\mathbf{r}_p^\perp) \rangle_{c'_p} \quad (3)$$

and  $l_p = c_p - c'_p$  is the distance of the  $p$ -port reference cross-section from the boundary of the scatterer. This  $c'_p$  cross-section choice for the calculation of the  $D$  overlaps is further justified in the Supplemental Material [47]. The  $P \times N$  matrices  $K$  and  $D$  quantify the couplings of the QNMs to the input and output CPM waves respectively, and they are generally frequency dependent. Eqs. (2) with  $\Omega$  diagonal (also known as state-space representation in diagonal canonical form in circuit theory [48]) constitute the basis of QNMT and their solution for the scattering matrix  $S$  is given by

$$S = C - D(i\omega - i\Omega)^{-1} K^t. \quad (4)$$

Although a general  $C(\omega)$  was included in Eqs. (2,4) to align with literature, we rely on the presumed completeness of the resonant QNMs to stipulate that each incident CPM wave is scattered to other CPMs only due to resonances. Therefore, for now, we take  $C$  as a diagonal phase matrix. Later, we will show that, indeed, low- $Q$  QNMs can be combined to write a general effective background  $C(\omega)$ ; in particular, a fully-transmissive  $C$  comes from a mode with infinite radiative rate (Appendix F).

*Shifts of ports’ reference cross-sections*— When  $S(\omega)$  is a meromorphic function, it is useful to use the Weierstrass factorization theorem and arguments from causality to write  $S = e^{i\tau\omega} S' e^{i\tau\omega}$ , where  $\tau$  is a constant diagonal matrix with real positive elements and  $S'$  is a “proper” rational function (Appendix A). Eq. (4) then implies that  $C(\omega) = C' e^{i2\tau\omega}$ ,  $D(\omega) = D' e^{i\tau\omega}$  and  $K(\omega) = K' e^{i\tau\omega}$ , where  $C'$  is a diagonal constant phase matrix that can be taken equal to  $I$  without loss of generality, and  $D'$ ,  $K'$  are now *constant* matrices.

This is indeed the case for CPMs with fields transverse to their direction of propagation ( $\phi_p \cdot \mathbf{k}_p = 0$ ), such as plane waves or dual-conductor TEM microwave modes, that are the focus of this article in filter design. They have  $k_p = \omega/v_p$  (where  $v_p$  the wave speed) and  $\phi_p^\perp(\mathbf{r}_p^\perp)$  independent of  $\omega$ , so Eq. (3) suggests that  $D_{pn}(\omega) = D'_{pn} e^{i\omega l_p/v_p}$  with  $D'_{pn}$  in fact constant. Thus, in all structures simulated in this article, we remove this linear phase to compute  $S'$ , referenced at the new port cross-sections  $c'_p$  on the scatterer boundary. In practice,  $\tau_{pp}$  may be slightly larger from  $l_p/v_p$ , adding a small constant group delay just to the phases of  $S$ , so it is of no

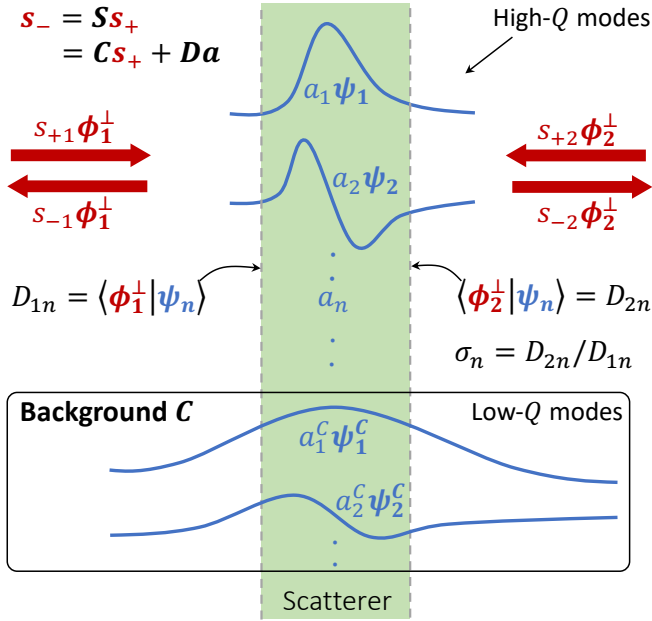


FIG. 1. A 2-port scattering system with important QNMT parameters. At excitation frequency  $\omega$ , the coupling port-modes (CPMs) with transverse fields  $\phi_p^\perp$  have input and output amplitudes respectively  $s_{\pm p}$ , related by the  $S$ -matrix through  $s_- = S s_+$ . The open scattering system supports quasi-normal modes (QNMs) with complex frequencies  $\omega_n$  and fields  $\psi_n$ , which have amplitudes  $a_n$  upon excitation. The CPM-to-QNM coupling coefficients are  $D_{pn}$ , with ratios  $\sigma_n = D_{2n}/D_{1n}$ . Imposing realness, unitarity, and symmetry constraints on  $S$  allows us to compute it as a function of only  $\omega_n$  and  $\sigma_n$  [Eq. (7)]. Optionally, by separating low- $Q$  modes  $\psi_n^c$ , we can also construct a slowly-varying background matrix  $C$ , which can give a physical intuition about the scattering response and help in specific filter designs.

concern for applications dependent only on their amplitudes (such as the amplitude filters we discuss in the next sections).

Therefore, hereafter we drop the  $'$  and consider  $S$  to be such a proper rational function that can be decomposed as

$$S = I - D(i\omega - i\Omega)^{-1} K^t \Leftrightarrow S_{pq} = \delta_{pq} - \sum_{n=1}^N \frac{D_{pn} K_{qn}}{i\omega - i\omega_n}. \quad (5)$$

For other types of CPMs,  $S(\omega)$  may not be meromorphic, for example when higher-order CPMs have a cut-off frequency, which appears as a branch-point [and frequency dependent  $D'(\omega)$ ,  $K'(\omega)$ ]. Such systems are not investigated in this work.

*Normalization independence*— Recall that measurable physical quantities (such as the  $S$ -matrix) do not depend on the choice of normalization for the QNM amplitudes  $\mathbf{a}$ . For example, it is easily seen from the QNMT Eqs. (2) that, for the fixed normalization of  $\mathbf{s}_\pm$ , two different sets  $(a_n, K_{qn}, D_{pn})$  and  $(a'_n, K'_{qn}, D'_{pn})$  scale as

$a'_n/a_n = K'_{qn}/K_{qn} = D_{pn}/D'_{pn}$ , hence  $S_{pq}$  in Eq. (5) is unchanged. Thus an overall scaling factor can be chosen arbitrarily for each QNM.

For some physical quantities analytically computed via the QNM fields, this normalization independence is typically ensured by dividing with the volume-integral norm  $\{\psi_n|\psi_n\}$  of these fields. However, since they are non-integrable, regularizing this norm is a cumbersome procedure that adds complexity [43]. As highlighted in Ref. 36 and we show also later, this phenomenological QNMT formulation does not require such norm evaluation, so it is simple and fast.

We now proceed by imposing constraints on  $S$ , based on the physical properties of the system.

*Realness*— For real input fields on a physical system, the output fields and thus the system response  $S(t)$  must also be real. In frequency domain, this realness of  $S$  is stated as  $S^*(i\omega) = S(-i\omega^*)$ . The same relation holds for the system Hamiltonian  $H$  verifying  $H(i\omega)\psi = i\omega\psi$ , so every QNM solution  $(\omega_n, \psi_n)$  is paired with another QNM  $(\omega_{n'}, \psi_{n'}) = (-\omega_n^*, \psi_n^*)$ . Similarly, the CPMs satisfy  $\phi_p^*(\omega) = \phi_p(-\omega^*) \Rightarrow \phi_p^{\perp*} = \phi_p^\perp$ . Eq. (3) thus shows that  $D_{pn'} = D_{pn}^*$ . Then, to satisfy  $S^*(i\omega) = S(-i\omega^*)$ , Eq. (5) requires also  $K_{pn'} = K_{pn}^*$ . Note,  $S$  realness implies that not only poles but also zeros of any  $S_{pq}$  appear in pairs  $(\omega_o, -\omega_o^*)$ , and that  $S_{pq}$  is a rational function of  $i\omega$  with real coefficients.

*Energy conservation*— In absence of absorption or gain, energy conservation implies that the  $S$  matrix is unitary ( $\mathbf{s}_+^\dagger \mathbf{s}_+ = \mathbf{s}_-^\dagger \mathbf{s}_- \Leftrightarrow S^\dagger S = I$ ) [32]. In Appendix B, we prove that a *necessary and sufficient* condition is given by

$$K = -D^* (M^t)^{-1}, \text{ with } M_{nl} = \frac{\sum_{p=1}^P D_{pl} D_{pn}^*}{i\omega_l - i\omega_n^*} = M_{ln}^*, \quad (6)$$

thus  $S$  can be written as

$$S = I + D(i\omega - i\Omega)^{-1} M^{-1} D^\dagger. \quad (7)$$

In Appendix C, we show that this Eq. (6) choice of  $K$  satisfies the realness requirement, namely, for  $D_{pn'} = D_{pn}^*$ , we get  $K_{pn'} = K_{pn}^*$ . In Appendix D, we rearrange Eq. (7) to show that  $S$  is fully and uniquely determined by the resonant frequencies  $\omega_n$  and the ratios  $\sigma_{r,pn} = D_{pn}/D_{r,n}$  (for some chosen port  $r_n$  for each mode  $n$ ). These quantities can be readily calculated using any appropriate eigenmode solver, where  $D_{pn}$  is determined by the surface integral in Eq. (3) and the ratios  $\sigma_{r,pn}$  remove the  $\psi_n$ -normalization-dependent scaling-factor. Therefore, as promised,  $S$  in Eq. (7) does not require computing the cumbersome volume-integral norms of the QNMs. Note also that Eq. (6) is different from the usual CMT expression of energy conservation  $D^\dagger D = 2|\text{Im}\{\Omega\}|$ , associated with modes orthonormal under the standard “energy” inner product, which does not hold for QNMs.

*Reciprocity*— Reciprocity implies that the  $S$  matrix is symmetric ( $S = S^t$ ) [32]. From Eq. (5), we can see that this is equivalent to having

$$\frac{K_{pn}}{D_{pn}} = \frac{K_{qn}}{D_{qn}} \Leftrightarrow K = D\Lambda \quad (8)$$

and therefore

$$S = I - D(i\omega - i\Omega)^{-1}\Lambda D^t \quad (9)$$

for some *arbitrary* diagonal matrix  $\Lambda$  with entries  $\lambda_n$  [with the only restriction that  $\lambda_{n'} = \lambda_n^* \neq 0$ , so that Eq. (8) is compatible with realness], where a specific choice of  $\lambda_n$  fixes the  $\psi_n$ -normalization-dependent scaling-factor. For any such choice, as mentioned earlier, the numerator of pole  $n$  for  $S_{pq}$  in Eq. (9) stays the same, however, its calculation requires evaluation/regularization of divergent volume integrals involving the QNM fields (including their norm  $\{\psi_n|\psi_n\}$ ), which we try to avoid here. Note also that, since  $\Lambda$  can be arbitrary, the usually assumed condition of reciprocity  $K = D$  (corresponding to the specific normalization choice  $\Lambda = I$ ) is *not necessarily* true.

*D-optimization*— In order to satisfy both energy conservation and reciprocity (unitarity and symmetry of  $S$ ), the input coupling coefficients  $K$  must satisfy both Eq. (6) and (8) simultaneously, namely the output coupling coefficients  $D$  must satisfy

$$D_{qn} \sum_l M_{nl}^{-1} D_{pl}^* = D_{pn} \sum_l M_{nl}^{-1} D_{ql}^* \Leftrightarrow D^* = -D\Lambda M^t. \quad (10)$$

Here again, for each resonance  $n$ , either  $D_{r_n n}$  (for one port  $r_n$ ) or  $\lambda_n$  can be chosen arbitrarily. In practice, this reciprocity condition Eq. (10) is a set of  $PN$  equations. Let  $D^c$  be the coupling coefficients computed from the eigenmode solver. In most cases, as we see in numerical examples, it turns out that  $D^c$  are very close to satisfying this required condition, but they don't satisfy it perfectly, since the finite set of chosen resonances is not truly complete. This is why in Ref. 36, Eq. (10) was not enforced exactly, rather the  $N$  coefficients of  $\Lambda$  were chosen to minimize its error and their final  $S$ -matrix, which was formulated as in Eq. (9), was reciprocal but not necessarily unitary. Instead, here, we give priority to exactly satisfying these physical properties of the actual system, if we want our model to be a physically realistic and thus, as we will show, a more accurate description. Therefore, we fine-tune the  $PN$  coefficients  $D$  by using a constrained optimization procedure, with the goal of exactly satisfying Eq. (10) while staying as close as possible to the computed system performance:

$$D = \underset{D^* = -D\Lambda M^t}{\operatorname{arg\,min}} f(D, D^c) \quad (11)$$

where  $f(D, D^c)$  is some penalty function to ensure that  $D$  stays close to  $D^c$  (note [49]). An obvious choice is  $f(D, D^c) = \|D - D^c\|^2$ . Another option is  $f(D, D^c) = \sum_{\{p,q\}} \|R_{pq}(D) - R_{pq}(D^c)\|^2$ , where  $R(D)$  represents the residues of the scattering matrix expansion given in Eq. (7) and  $\{p, q\}$  a chosen subset of indices. When summing over  $p \neq q$ , the global optimum is reached for  $D$  satisfying  $R_{pq}(D) = R_{qp}(D) = [R_{pq}(D^c) + R_{qp}(D^c)]/2$ , but such a set of  $D$  is not guaranteed to exist. When it does exist, directly solving for this system of equations has given the best results in our experience with actual 2-port systems.

*Properties of 2-port systems*— Since the most common applications of scattering theory, including the ones examined in this article, involve 2-port systems, we discuss some properties of their  $S$  matrix.

Energy conservation leads to the unitary  $S$ -matrix of Eq. (7), which is recast in normalization-independent form for a 2-port in Eq. (D3). Realness requires that, for each mode  $(\omega_n, \sigma_n)$ , where  $\sigma_n = D_{2n}/D_{1n}$ , the mode  $(-\omega_n^*, \sigma_n^*)$  is also included. Then, the dependence of  $S$  on  $\sigma_n$  can be easily checked to satisfy, for  $\gamma = \pm 1$ ,

$$\begin{aligned} S_{11\{\omega_n, \gamma\sigma_n\}} &= S_{11\{\omega_n, \sigma_n\}}, & S_{12\{\omega_n, \gamma\sigma_n\}} &= \gamma^* S_{12\{\omega_n, \sigma_n\}} \\ S_{21\{\omega_n, \gamma\sigma_n\}} &= \gamma S_{21\{\omega_n, \sigma_n\}}, & S_{22\{\omega_n, \gamma\sigma_n\}} &= S_{22\{\omega_n, \sigma_n\}}. \end{aligned} \quad (12)$$

[If only positive-frequency modes are considered and thus the realness requirement is relaxed—commonly known as a rotating-wave approximation (RWA)—Eq. (12) holds for any phase factor  $\gamma = e^{i\varphi}$ .] Moreover, swapping ports  $1 \leftrightarrow 2$  corresponds simply to replacing  $\sigma_n \leftrightarrow 1/\sigma_n$ :

$$S_{11\{\omega_n, \sigma_n\}} = S_{22\{\omega_n, 1/\sigma_n\}}, \quad S_{21\{\omega_n, \sigma_n\}} = S_{12\{\omega_n, 1/\sigma_n\}}. \quad (13)$$

As a consequence, when all  $\sigma_n$  are  $\pm 1$  (as for a symmetric structure, whose modes must be even or odd [50]),  $S_{11} = S_{22}$  and  $S_{21} = S_{12}$ , so the 2-port system is immediately reciprocal. (Obviously,  $\sigma_n = \pm 1$  is not *necessary* for the reciprocity condition Eq. (10) to hold.) Note that energy conservation alone implies that  $|S_{12}| = |S_{21}|$ , so reciprocity in lossless 2-ports is mostly a statement on the transmission phase responses.

Finally, in Appendix E, it is shown for a real lossless reciprocal 2-port system that (i) the zeros of  $S_{21}$  can only appear as complex quadruplets  $(\omega_o, \omega_o^*, -\omega_o, -\omega_o^*)$ , real or imaginary pairs  $(\omega_o, -\omega_o)$ , or at  $\omega_o = 0$  and that (ii), for each zero-pair  $(\omega_o, -\omega_o^*)$  of  $S_{11}$ ,  $(-\omega_o, \omega_o^*)$  is a zero-pair of  $S_{22}$ . The restrictions (i) on the  $S_{21}$  zeros imply that its numerator is a polynomial of  $\omega^2$  with real coefficients, optionally with multiplicative  $i\omega$  factors.

*Absorption and gain*— In presence of small absorption loss,  $S$  is no longer unitary, but it can be calculated perturbatively when all relevant modes have high  $Q$ . For this, we decompose loss rates into radiative ( $\Gamma_r$ ) and non-radiative ( $\Gamma_{nr}$ ) parts, and perturbatively compute coefficients in Eq. (7). While the denominators have a first-order change in  $\Gamma_{nr}$  ( $\omega - \Omega$  becomes

$\omega - \Omega + i\Gamma_{\text{nr}}$ , the numerators scale as  $DM^{-1}D \sim \Gamma_r$  and become  $\sim \Gamma_r(1 + \text{const} \cdot \Gamma_{\text{nr}})$  [no scattering when  $\Gamma_r \rightarrow 0$ ]. We then see that, for high- $Q$  modes (where both  $\Gamma_r$  and  $\Gamma_{\text{nr}}$  are small), to first order in  $\Gamma_{r,\text{nr}}$ , the numerators in Eq. (7) are equal to those of the lossless case, while the absorption loss rates still affect the poles. (A similar argument is often implicitly used in CMT, where it is typically assumed that  $\Gamma = D^\dagger D + \Gamma_{\text{nr}}$  with  $D$  not changing in the presence of  $\Gamma_{\text{nr}}$  because  $\Gamma$  itself is small [36], or is explicitly used to argue that the coupling coefficients to different CMT channels can be determined independently [50].) In summary, for weakly absorptive (or even active) scatterers, we compute  $S$  using Eq. (7), where loss (or gain) rates are included in  $\Omega$  but not in  $M$ . Since the lossless-case  $D$  was fine-tuned for reciprocity, the non-unitary  $S$  will still be symmetric. While the perturbation argument assumes high- $Q$  modes, in practice it seems to often hold even when relatively low- $Q$  modes are present, as we see in the next metasurface example.

## B. Examples in electromagnetism

*Normal incidence on microwave metasurface*— To examine the accuracy of our QNMT, we now study scattering of an electromagnetic plane wave normally incident on the metasurface at a frequency  $f = \omega/2\pi$ , depicted in the inset of Fig. 2(a). It consists of alternating dielectric (green) and metallic (grey) layers, where the latter have been etched out to form two-dimensional square periodic lattices of thin metallic crosses and a square air-hole has been etched throughout the entire thickness  $\tilde{t}$  of the metasurface in the region between the crosses.

Unless otherwise noted, in all microwave metasurfaces studied in this article: (i) The metal thickness is  $18\mu\text{m}$  (corresponding to  $0.5\text{oz}$  copper). (ii) The square-lattice period  $a$  and the centers of the crosses are the same for all patterned layers. (iii) We study for frequencies below the first diffraction cutoff ( $f_{\text{cut}} = c/a$  at normal incidence), so only transmission and reflection need to be considered. (iv) There is  $C_{2v}$  symmetry, so the response for normal incidence is independent of the polarization  $\hat{e}$  and only 2 ports are needed. (v) Numerical computation of the “exact” frequency response ( $S$ -matrix) for plane-wave excitation as well as of the eigenmodes for use in our QNMT is carried out using COMSOL Multiphysics [51]. (vi) Complex eigenfrequencies  $\omega_n$  are immediately obtained from the eigensolver, while the coupling coefficients  $D_{1n}$ ,  $D_{2n}$  are computed from Eq. (3) as “power” inner-product surface integrals

$$D_{pn} \propto \int_{c'_p} (\mathbf{E}_p^* \times \mathbf{H}_n + \mathbf{E}_n \times \mathbf{H}_p^*) \cdot d\mathbf{S} \quad (14)$$

at the two (left/right for  $p = 1, 2$ ) external boundaries of the scatterer between the QNM field  $\psi_n = (\mathbf{E}_n, \mathbf{H}_n)$  and the coupling port-modes  $\phi_p^\perp = (\mathbf{E}_p, \mathbf{H}_p)$  [plane waves in

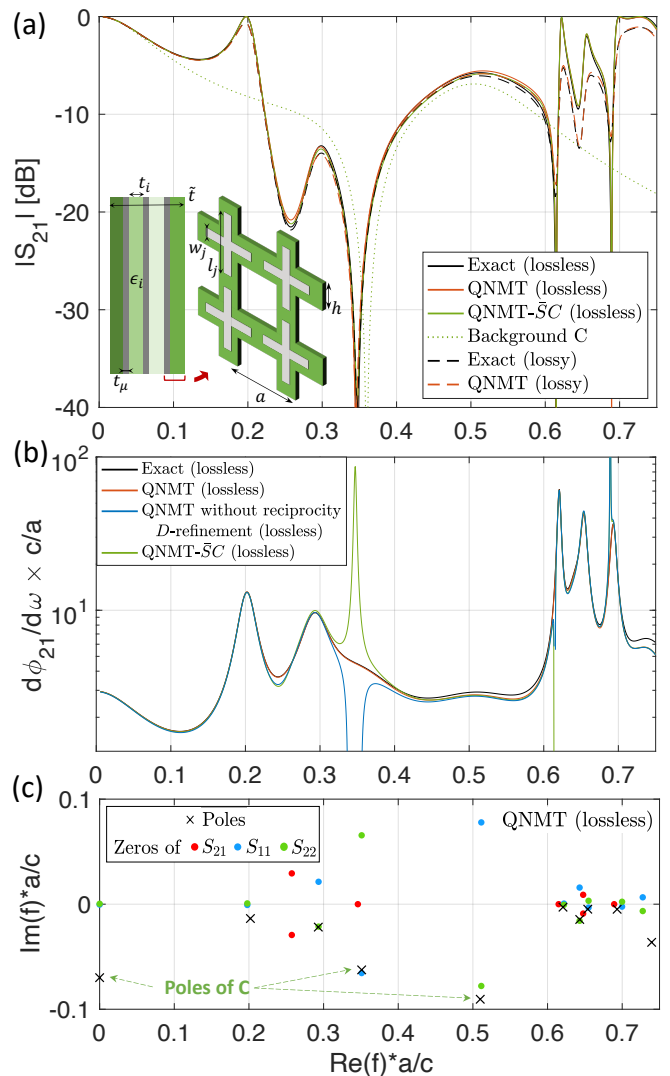


FIG. 2. QNMT modeling scattering of a plane wave normally incident from the left on the metasurface depicted in the inset of (a). Parameters (listed from left to right) are:  $a = 15\text{mm}$ ,  $h/a = 0.64$ ,  $w/a = (0.05, 0.2, 0.1)$ ,  $l/a = (0.62, 0.92, 0.82)$ , metal (grey) layers’ thickness  $t_\mu = 18\mu\text{m}$ , dielectric (green) layers’ permittivities  $\epsilon = (4, 6, 3, 10)$  and thicknesses  $t/a = (0.1, 0.2, 0.3, 0.2)$ . In the lossy simulation, we used copper and added loss  $\tan\delta = 0.01$  to all dielectric layers. Curves: (a) magnitude and (b) group delay of the transmission coefficient (where a constant delay of  $0.19 \times a/c$  was added to QNMT to match the exact simulation at low frequencies). (c) Lossless-system poles used in the QNM expansion and zeros of the resulting  $S$  coefficients, confirming unitarity and symmetry of  $S$ . The dotted arrows point at the 3 modes used to compute the slowly varying background  $C$  in the  $S = \bar{S}C$  approximation. Agreement with our corrected QNMT is very good in both lossless and lossy structures.

this case, so  $D_{pn} \propto \int_{c'_p} (\hat{e} \cdot \mathbf{E}_n) dS$ , where, as emphasized earlier, only their ratio  $\sigma_n$  is needed. In the Supplemental Material [47], we provide further details and guidelines for the numerical simulations (mainly how to

avoid spurious modes [52–55]), as well as tables with the calculated eigenmodes for every structure presented in the article.

For the asymmetric structure of Fig. 2, the parameters were chosen arbitrarily to test a very general response, with  $\sigma_n$  departing substantially from  $\pm 1$ . Even so, we see a very good match between the exact numerical computation (black lines) and the QNM expansion of Eq. (7) (red lines), in both cases of the metal being a perfect electric conductor (PEC) (solid lines) or copper (dashed lines). The copper merely reduces transmission by few dB at high frequencies, while maintaining the same overall features. Therefore, for the rest of the article, most of our design structures will use PEC. In this lossless case, we emphasize again that, due to our symmetrization procedure of Eq. (11), the QNM expansion we obtained is both unitary and symmetric. This is why the zeros of  $S_{21} = S_{12}$  are either real or complex conjugate pairs, and the zeros of  $S_{11}$ ,  $S_{22}$  complex conjugates of each other, as they should [Fig. 2(c)]. As mentioned earlier, this affects the accuracy of the phase response of the predicted  $S$ . In Fig. 2(b), the group delay of  $S_{21}$  before our symmetrization process is shown to have dramatic errors in frequency regions close to inaccurately non-real zeros (even leading to non-causal negative delay), which are removed after imposing Eq. (10).

One key advantage of the QNMT method is that it resolves spectra around very-high- $Q$  modes with perfect detail, while a frequency simulation requires a very dense uniform frequency-grid to resolve them, being ignorant of their location. This, in turn, leads to a stark benefit in speed for QNMT. For this example, on the same machine and finite-element mesh, the QNMT calculation took an average of  $\sim 60$  secs per mode ( $\times 10$  modes in Fig. 2), while the frequency-domain calculation an average of  $\sim 100$  secs per point ( $\times 600$  points in Fig. 2).

*4-port metasurface via coupled polarizations*— For a  $P$ -port system with  $P > 2$ , unitarity alone does not guarantee  $|S_{pq}| = |S_{qp}|$  anymore, so our method of fine-tuning the  $D$  coefficients to also enforce reciprocity [Eq. (11)] corrects errors not just in the scattering phase, but in the amplitudes too.

To demonstrate this advantage, we also study a microwave metasurface with three dielectric layers sandwiching two metallic sheets, with patterned arrays of *rotated* cross-like apertures [inset of Fig. 3(a)]. This structure does not have the required symmetry for the normally incident plane-wave polarization to be conserved, instead the two orthogonal polarizations on each side cross-couple in both reflection and transmission, so a 4-port system is needed. In Fig. 3(a), we plot  $|S_{34}|$  and  $|S_{43}|$ , which are nonphysically different before the fine-tuning (blue lines), but become equal after our method (red lines) and closer to the exact result (black lines). The other scattering amplitudes and the structural parameters are shown in the Supplemental Material [47].

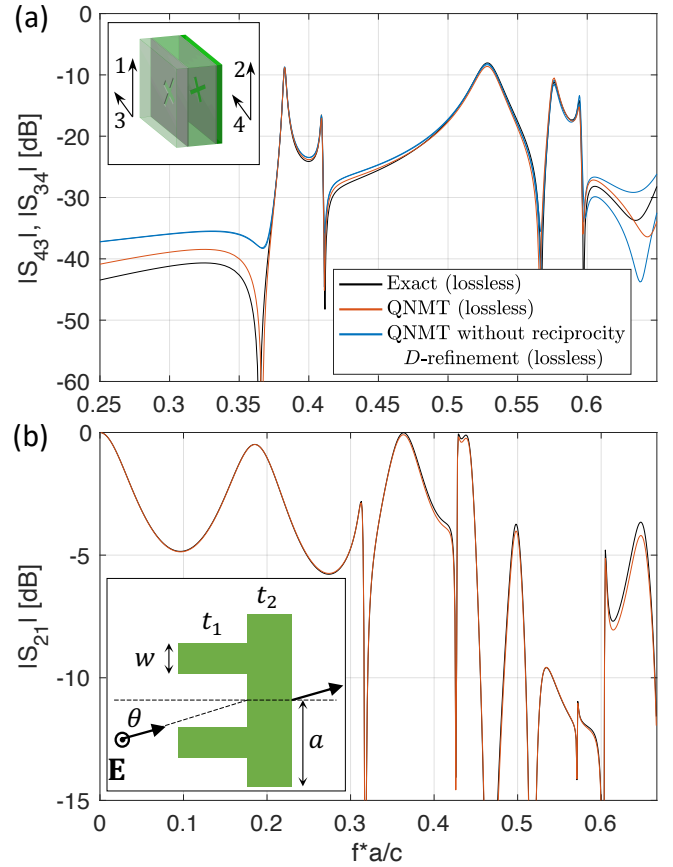


FIG. 3. QNMT modeling of: (a) Transmission of one polarization of a normally incident plane wave from a metasurface with rotated apertures (structural details in Supplemental Material [47]). Note that  $|S_{34}| \neq |S_{43}|$  for  $D$  satisfying unitarity but not symmetry (blue lines), which is then corrected with our method (red lines). (b) Transmission of obliquely incident ( $\theta = 30^\circ$ ) TE plane wave from a dielectric ( $\epsilon = 11$ ) grating with  $w/a = 0.4$  and  $(t_1, t_2)/a = (0.4, 0.3)$ .

*Oblique incidence on 2d photonic metasurface*— When a plane wave is incident on a metasurface at an angle  $\theta$ , its transverse wavevector component at frequency  $\omega$  is  $k^\perp = \omega \sin\theta/c$ . Phase matching then imposes that this must also be the Bloch wavevector within the metasurface. QNMT modeling with such excitation may seem intractable at first glance, if one tries to obtain a full band diagram to apply QNMT at each fixed real  $k^\perp$ . However, we show here that the relevant QNMs are those calculated from a *nonlinear* eigenproblem, where the phase matching condition is imposed at the complex eigenfrequency by analytic continuation (thus giving a complex Bloch wavevector  $k_n^\perp = \omega_n \sin\theta/c$ ). To find such unusual resonances, we developed software for two-dimensional (2d) dielectric structures, whose geometry can be split into uniform layered sections: at any complex  $\omega$ , these complex Bloch modes are calculated within each section with a  $T$ -matrix formulation, then matched at interfaces between sections, and finally radiation conditions are applied to find the resonances (similar to CAMFR [56] and

other interface mode-matching analyses [57, 58]).

We then study scattering of a plane wave incident at a  $30^\circ$  angle on a 2d photonic grating with its  $\mathbf{E}$ -field transverse to the plane [inset of Fig. 3(b)]. For frequencies below the first diffraction cutoff  $f_{\text{cut}} = c/a(1 + \sin\theta)$ , the system again has only 2 ports. In Fig. 3(b), we show transmission, calculated both exactly (same software used at real  $\omega$ ) and with our QNMT. The agreement is indeed very good all throughout the range.

### C. Background scattering via low- $Q$ modes

In some design situations (as we show in later examples), one needs an effective slowly-varying background response, which has to be designed collectively and in conjunction with the high- $Q$  modes. This background response (responsible also for the concept of Fano resonances [59]) is usually modeled in standard CMT via the direct-coupling matrix  $C$  in Eq. (2). In most cases, researchers have approximated  $C$  by simulating an effective background structure derived by some type of topology averaging, which removes the high- $Q$  resonances, and its parameters were chosen (always, so far, to our knowledge) *a posteriori* for a best fit [33, 34]. Here, we show how  $C$  can be calculated using the actual structure under study by appropriately combining its low- $Q$  modes and then how the total  $S$  can be computed.

Consider a lossless system supporting some high- $Q$  resonant modes ( $\omega_n = \Omega_n - i\Gamma_n$ ), while the rest ( $\omega_n^C = \Omega_n^C - i\Gamma_n^C$ ) have much smaller  $Q$  (Fig. 1). Starting from Eq. (5), we combine these low- $Q$ -mode terms within the sum to define  $C(\omega) \equiv S_{\{\omega_n^C\}}(\omega)$ , so that  $S$  takes the form of Eq. (4), with  $\Omega$  including only the high- $Q$  modes. In the limit  $\Gamma^C \rightarrow \infty$ ,  $C$  becomes a frequency-independent matrix, which is unitary, since  $S(\omega \rightarrow \infty) = C$ . Therefore, we can use Eqs. (6),(7) to calculate  $C$  and Eq. (11) to guarantee its symmetry. In this process,  $M_{nl}^C \approx \sum_{p=1}^P D_{pl}^C D_{qn}^{C*} / (\Gamma_l^C + \Gamma_n^C)$ , so the  $\Gamma_n^C \rightarrow \infty$  cancel out between  $M^C$  and the  $C$ -denominator poles, leading to a constant  $C$  not necessarily equal to  $I$ . As a useful example, in Appendix F, we show that, in a 2-port system, a single such  $\Gamma_n^C \rightarrow \infty$  mode with  $\sigma = -1/t \pm \sqrt{1/t^2 - 1}$  gives a constant background transmission  $C_{21} = t$ . Now, for the total  $S$ -matrix of Eq. (4), following the same procedure of Appendix B but with  $I$  replaced by a unitary symmetric constant  $C$ , one can easily see that  $S^\dagger S = I$  is now equivalent to  $K^t = -M^{-1}D^\dagger C$ . Therefore, the constant background  $C$  can be factored out of Eq. (4) to write:

$$\begin{aligned} S &= \bar{S}C = [I - D(i\omega - i\Omega)^{-1}M^{-1}D^\dagger] C \\ \Leftrightarrow S_{pq} &= C_{pq} - \sum_n \frac{D_{pn} \sum_l M_{nl}^{-1} \sum_r D_{rl}^* C_{rq}}{i\omega - i\omega_n}. \end{aligned} \quad (15)$$

Here,  $\bar{S}$  has the form of a separate scattering matrix, which itself also satisfies realness, unitarity and the properties of Eqs. (12, 13). The condition of Eq. (10), to additionally impose exact symmetry on  $S$ , is modified to

$$\begin{aligned} D_{qn} \sum_l M_{nl}^{-1} \sum_r D_{rl}^* C_{rp} &= D_{pn} \sum_l M_{nl}^{-1} \sum_r D_{rl}^* C_{rq} \\ \Leftrightarrow CD^* &= -D\Lambda M^t, \end{aligned} \quad (16)$$

through which a fine-tuned  $D$  can be evaluated by an optimization procedure, as before, to obtain the final  $S$ .

In practice, however, real systems have modes with low but nonzero  $Q$ . (In fact, as we discuss in the Supplemental Material [47], very-low  $Q$  modes are very difficult to locate numerically anyway.) Therefore, realistically,  $C(\omega)$  is slowly varying instead of constant and is *not* necessarily unitary (as it does not describe a physical system by itself). Nevertheless, we can still use Eq. (7) for those low- $Q$  modes to obtain a unitary (thus approximate)  $C$  and then use Eq. (15) with the high- $Q$  modes inside  $\bar{S}$  to get  $S$  simply as a best-effort *approximation* to the actual system response. This  $\bar{S}C$  construction still guarantees that  $S$  will also satisfy realness  $S^*(\omega) = \bar{S}^*(\omega)C^*(\omega) = \bar{S}(-\omega^*)C(-\omega^*) = S(-\omega^*)$  and unitarity ( $S^\dagger S = C^\dagger \bar{S}^\dagger \bar{S} C = I$ ), but does *not* guarantee reciprocity ( $S^t = C^t \bar{S}^t \neq \bar{S} C = S$ ) [although unitarity at least implies  $|S_{12}| = |S_{21}|$  for a 2-port]. Attempts to symmetrize  $S$  (for example [60]) are not expected to have much success: if it were possible to exactly satisfy also reciprocity for a varying  $C(\omega)$ , one would then be able to build a unitary and symmetric  $S$  by multiplying unitary and symmetric  $C$  matrices formed by individual modes, which obviously is not possible. Regardless,  $\bar{S}C$  is a good enough approximation (expected to get better with a slower-varying  $C$  and a larger number of modes in  $\bar{S}$ ), which we will show to be very helpful in filter design.

We can now test this formulation on the structure presented in Fig. 2. Using the three modes with lowest  $Q$ s (much lower than the other modes) to construct the  $C$ -matrix, we see that  $C_{21}$  indeed defines a slowly-varying transmission background (dotted line). Sharp features in  $S_{21}$  are then obtained by the high- $Q$  modes within the  $\bar{S}C$  formulation (green line), which actually gives a very good approximation of the overall transmission amplitude spectrum, with only small errors in the phase-delay prediction due to the remaining asymmetry of  $\bar{S}C$ .

### D. Summary

Resonant QNMs with frequencies  $\omega_n$  are computed with an adequate eigensolver. Coupling coefficients  $D_{pn}$  are computed as surface overlaps between normalized-CPM and non-normalized-QNM fields (as only ratios  $\sigma_{r,pn} = D_{pn}/D_{rn}$  are needed). Negative-frequency

modes  $(-\omega_n^*, D_{pn}^*)$  are included.  $D_{pn}$  are adjusted through Eq. (11).  $S$  is computed through Eq. (7). If desired,  $C$  is determined by the same procedure using only the low- $Q$  resonances,  $\bar{S}$  by using the high- $Q$  modes, and then  $S = \bar{S}C$ . The agreement of our QNMT with exact simulations gives us confidence that it can be successfully employed for rapid device design.

### III. FILTER DESIGN

The main goal of our work is to design physical 2-port systems with standard network-synthesis filter responses, specifically  $N$ th-order band-pass and band-stop filters of a finite bandwidth, which are given as rational functions of frequency  $H(\omega)$  with specified  $2N$  complex poles [appearing as  $N$   $(\omega_n, -\omega_n^*)$  pairs],  $2N$  zeros (abiding by the restrictions of Appendix E) and an overall constant. Attempting this design by optimizing over structural parameters to find a scattering-matrix that matches specific values of the desired  $H(\omega)$  at a finite set of key frequencies can be very difficult in practice, as this highly-resonant problem can present a vast number of local extrema and lead to “stiff” constraints [45]. Instead, the eigenmode-solver-derived components of a QNMT expansion have a much slower dependence on the physical structural parameters, so they yield a more tractable optimization formulation. Using our formulation from the previous section, it is obvious that the complex resonant frequencies of the physical system must match the complex poles of the desired filter. In this work, we show how to also enforce the desired zeros in the system response, by deriving the corresponding  $D$  coefficients and the matrix  $C$ . Specifically,  $|C_{21}|$  must match the desired filter background transmission and then, for exact ISFs, we find that the ratios of couplings of the QNMs’ fields to the two ports must be  $\sigma_n = \pm 1$  for  $N$  odd or  $\sigma_n = \pm i$  for  $N$  even, with alternating signs for consecutive modes. Enforcing  $|C_{21}|$  and the  $N$  complex  $\omega_n, \sigma_n$  results in a minimal set of  $4N + 1$  real equations. We also explain that good approximate solutions can be obtained, if an overall common phase for all  $\sigma_n$  is allowed, according to Eqs. (23–26).

*Symmetric and antimetric filters*— We explained that, for a general lossless reciprocal 2-port system, the zeros of  $S_{11}$  and  $S_{22}$  are conjugates of each other, but they do not necessarily coincide. In this article, we are interested in the special cases of filters where they do coincide, so that these zeros can only appear as complex quadruplets  $(\omega_o, \omega_o^*, -\omega_o, -\omega_o^*)$ , real or imaginary pairs  $(\omega_o, -\omega_o)$ , or at  $\omega_o = 0$ . Their numerator is then also (as is always true for  $S_{21}$ ) a polynomial of  $\omega^2$  with real coefficients, optionally with multiplicative  $i\omega$  factors. These cases include, in particular, common practical amplitude filters, for which all zeros of reflection ( $S_{11}$  and  $S_{22}$ ), corresponding to full transmission, lie on the real frequency axis or at infinity. To satisfy realness, this

class of filters is collectively described by the condition  $S_{22} = \pm S_{11}$ , namely they are either symmetric or “antimetric” [35] (note [61]). Energy conservation and reciprocity then force  $\sqrt{\gamma}S_{11}S_{21}^*$  to be purely imaginary for  $\gamma \equiv S_{22}/S_{11} = \pm 1$ , corresponding to (+) odd or (-) even number of  $i\omega$  factors in the numerator of  $S_{11}$  or  $S_{21}$ .

The most important subclass comprises the ideal standard filter (ISF) approximations [1]: Butterworth (flat passband and stopband), Chebyshev (equiripple passband, flat stopband), inverse Chebyshev (equiripple stopband, flat passband) and elliptic (equiripple passband and stopband) (see Fig. 6). For a  $N^{\text{th}}$ -order Butterworth or Chebyshev transmission bandpass filter,  $S_{21}$  has  $N$  zeros at  $\omega = 0$  ( $N$   $i\omega$ -factors in numerator) and  $N$  zeros at  $\omega \rightarrow \infty$  ( $2N$  zeros total). For  $N^{\text{th}}$ -order inverse Chebyshev or elliptic filters, which have zeros at finite real frequencies,  $S_{21}$  still has one zero at  $\omega = 0$  and one at  $\omega \rightarrow \infty$  for  $N$  odd, while all  $2N$  zeros are finite for  $N$  even (no  $i\omega$  factors). For a transmission bandstop filter, the same observations hold instead for  $S_{11}$ . In all ISF cases, we conclude that  $S_{11}S_{21}^*$  is purely imaginary ( $\gamma = 1$ ), if  $N$  is odd, and purely real ( $\gamma = -1$ ), if  $N$  is even.

*Conditions on C and D*— A partial-fraction expansion of the desired network-synthesis expresses  $H(\omega)$  in terms of the complex poles, their residues, and a direct term  $t$  (which gives the limiting response at high frequencies according to the filter’s type). Using the  $S = \bar{S}C$  formulation of Eq. (15) for an actual physical system, we assume that  $C$  can be designed as approximately constant over the finite bandwidth of interest, where it can generally be complex. Far from the high- $Q$  resonances ( $\omega \gg |\omega_n|$ ), Eq. (15) dictates  $\bar{S} \rightarrow I$  and thus  $S \rightarrow C$ . Therefore, for a transmission filter, one must design  $|C_{21}| = t$ . This provides design intuition for the topology of the structure, where appropriate low- $Q$  modes are utilized to get the desired  $C$ , as we will see in practical examples later. During structural optimization, it may be difficult to find the low- $Q$  modes contributing to  $C$ , in which case it can also be calculated efficiently as  $C = \bar{S}^{-1}S$ , where  $S$  is obtained via direct simulation of the structure (with the ports’ reference cross-sections shifted to the metasurface boundaries) and the filter-relevant high- $Q$  modes are used to get a QNMT evaluation of  $\bar{S}$ .

For the class of filters of interest with  $S_{22} = \gamma S_{11}$  ( $\gamma = \pm 1$ ),  $S \rightarrow C$  means that the unitary symmetric  $C$  also satisfies  $C_{22} = \gamma C_{11}$  and that  $\sqrt{\gamma}C_{11}C_{21}^*$  is purely imaginary. Now, since  $\bar{S} = SC^{-1}$ , we can write:

$$\bar{S} = \frac{1}{|C|} \begin{pmatrix} S_{11}\gamma C_{11} - S_{21}C_{21} & -S_{11}C_{21} + S_{21}C_{11} \\ S_{21}\gamma C_{11} - \gamma S_{11}C_{21} & -S_{21}C_{21} + \gamma S_{11}C_{11} \end{pmatrix} \quad (17)$$

so that  $\bar{S}_{11} = \bar{S}_{22}$  and  $\bar{S}_{21} = \gamma \bar{S}_{12}$ . Further using Eqs. (12, 13) for the dependence of  $\bar{S}$  on  $\sigma_n = D_{2n}/D_{1n}$ :

$$\begin{aligned}\bar{S}_{11}\{\omega_n, \frac{1}{\sigma_n}\} &= \bar{S}_{22}\{\omega_n, \sigma_n\} = \bar{S}_{11}\{\omega_n, \sigma_n\} = \bar{S}_{11}\{\omega_n, \frac{\sigma_n}{\gamma}\} \\ \bar{S}_{21}\{\omega_n, \frac{1}{\sigma_n}\} &= \bar{S}_{12}\{\omega_n, \sigma_n\} = \frac{1}{\gamma} \bar{S}_{21}\{\omega_n, \sigma_n\} = \bar{S}_{21}\{\omega_n, \frac{\sigma_n}{\gamma}\}.\end{aligned}\quad (18)$$

The same result applies to  $\bar{S}_{22}$  and  $\bar{S}_{21}$ , so we obtain  $\bar{S}_{\{\omega_n, 1/\sigma_n\}} = \bar{S}_{\{\omega_n, \sigma_n/\gamma\}}$ . From the uniqueness property shown in Appendix D, we conclude that  $1/\sigma_n = \sigma_n/\gamma$ . Therefore, for a lossless reciprocal 2-port system:

$$S_{22} = \gamma S_{11} \Leftrightarrow \sigma_n = \pm\sqrt{\gamma}, \quad (19)$$

so that all modes have  $\sigma_n = \pm 1$  for a symmetric filter ( $\gamma = 1$ ), while  $\sigma_n = \pm i$  for an antimetric ( $\gamma = -1$ ). (This generalizes the well-known CMT result for a single resonance, where transmission reaches 1 only for equal decay rates into the two ports [50].) Moreover, with this  $\sigma_n$  choice,  $i\sigma_n C_{11} C_{21}^*$  is purely real.

In the particular case of ISFs,  $C$  is constant over all frequencies, so it must be real, to satisfy the realness condition. Consistently with  $i\sigma_n C_{11} C_{21}^*$  real, odd-order ISFs have  $\sigma_n = \pm 1$  and  $C_{11} C_{21} = 0$ , while  $\sigma_n = \pm i$  for even order.

As detailed in the Supplemental Material [47], Eq. (19) can be also derived using general arguments based on the transfer matrix. However, our QNMT further helps specify the choice of  $\sigma$ -signs to enforce the desired positions of  $S$ -coefficients zeros, as we show in the remainder of this section.

*Types of Filters*— For each mode  $n$ , the appropriate choice of sign for  $\sigma_n$  in Eq. (19) depends on the specific filter type that is being designed. We find the adequate choice analytically in the limit of large  $Q$ s, or more specifically when  $\Gamma_{n,l} \ll |\Omega_n - \Omega_l|$  for  $\omega_n = \Omega_n - i\Gamma_n$ . Under such condition, the matrix  $M$  is dominated by its diagonal terms  $M_{nn} = (1 + |\sigma_n|^2)/2\Gamma_n$ , so [see Eq. (D3)]:

$$\bar{S}_{pq} \approx \delta_{pq} + \sum_n \frac{\Gamma_n}{i(\omega - \Omega_n) - \Gamma_n} \frac{2\sigma_{pn}\sigma_{qn}^*}{1 + |\sigma_n|^2}, \quad (20)$$

with  $\sigma_{1n} = 1$ ,  $\sigma_{2n} = \sigma_n$ . Then, away from the resonances ( $\Gamma_n \ll |\omega - \Omega_n|$ ) and to lowest order in  $\Gamma_n$ , further using  $|\sigma_n| = 1$  from Eq. (19), transmission is

$$S_{21} \approx C_{21} - i \sum_n \frac{\Gamma_n}{\omega - \Omega_n} (\sigma_n C_{11} + C_{21}). \quad (21)$$

As the overall background transmission  $C_{21} \approx S_{21}(\omega \gg \Omega_n)$  determines the filter type, we will study its different cases separately.

**Case (a)**  $C_{21} = 0 \Leftrightarrow |C_{11}| = 1$ : This is a band-pass filter with zero transmission at  $\omega \rightarrow \infty$ . From Eq. (21), we have  $S_{21} \propto \sum_n \Gamma_n \sigma_n / (\omega - \Omega_n)$ , which, under condition Eq. (19), is proportional to a real function that can be easily used to determine the placement of its zeros. As

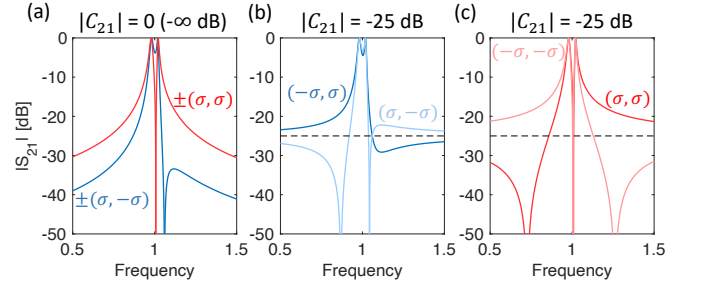


FIG. 4. Second-order filter responses, using QNM expansions of the form  $S = \bar{S}C$ , with two modes of frequencies  $\Omega = (0.98 - 0.01i, 1.02 - 0.005i)$  and coupling ratios  $(\pm\sigma, \pm\sigma)$  in  $\bar{S}$ , and with unitary reciprocal  $C = \begin{pmatrix} i\sigma^* r & t \\ t & i\sigma r \end{pmatrix}$  where  $r = \sqrt{1 - t^2}$  and such that  $\beta = i\sigma^*$  and  $C_{22} = \sigma^2 C_{11}$  ( $\Leftrightarrow S_{22} = \sigma^2 S_{11}$ ), for different values of real background transmission  $t$  indicated in the plots. We use the RWA of ignoring negative-frequency poles, so the amplitudes of  $S$ -matrix coefficients are exactly the same for any complex  $\sigma = \sqrt{\gamma} = e^{i\varphi/2}$ . A zero always occurs between modes of same coupling ratio (red), so filters with no zeros between the poles require opposite signs of the ratios (blue). Including negative-frequency poles would result to the same qualitative behavior and only slightly change the response away from the resonances.

an example, we look at the simple scenario of two modes with  $\Omega_1 < \Omega_2$  and calculate the zero at

$$\omega_o \approx \frac{\Omega_2 \Gamma_1 \sigma_1 + \Omega_1 \Gamma_2 \sigma_2}{\Gamma_1 \sigma_1 + \Gamma_2 \sigma_2}. \quad (22)$$

One can easily confirm that, when  $\sigma_1 = \sigma_2$ , the zero appears between the modes ( $\Omega_1 < \omega_o < \Omega_2$ ), a feature often observed in interference phenomena, such as electromagnetically induced transparency (EIT) [38, 62]. When  $\sigma_1 = -\sigma_2$ , it appears on the side of the mode with the smallest loss rate ( $\omega_o < \Omega_1$  if  $\Gamma_1 < \Gamma_2$  and  $\omega_o > \Omega_2$  if  $\Gamma_2 < \Gamma_1$ ), while there is no zero if  $\Gamma_2 = \Gamma_1$  [explaining the lack of transmission zeros predicted by traditional CMT for two equal-loss coupled resonances [34] and in symmetric ‘‘Fabry-Perot’’ systems where all  $\Gamma$ ’s are the same (Appendix F)]. These points are illustrated in Figure 4(a).

These conclusions can be extended to the scenario of multiple high- $Q$  modes: a real zero always occurs between two consecutive modes of same  $\sigma_n$ , there can only be an even (or zero) number of real zeros between two consecutive modes of opposite  $\sigma_n$  and, below the lowest mode or above the highest mode, a zero can exist only if there is at least one change in  $\sigma$ -sign.

For the ISFs with no transmission at infinity, such as a Butterworth, Chebyshev, odd-order inverse Chebyshev or odd-order elliptic, where the transmission zeros are always outside the passband, it is necessary to design  $\sigma_n$  with alternating signs, namely

$$\sigma_n = \pm\sqrt{\gamma} (1, -1, 1, -1, \dots) = \pm\sqrt{\gamma} (-1)^{n-1}. \quad (23)$$

**Case (b)**  $0 < |C_{21}| \ll |C_{11}| < 1$ : This is a band-pass filter with finite small transmission at  $\omega \rightarrow \infty$ . From Eq. (21), we have  $S_{21} \approx C_{21} - iC_{11} \sum_n \Gamma_n \sigma_n / (\omega - \Omega_n)$ . If we denote  $\beta = C_{11} C_{21}^* / |C_{11} C_{21}|$ , then, from the previous discussion,  $i\sigma_n \beta = \pm i\sqrt{\gamma} \beta = \pm 1$ . Therefore,  $S_{21}$  is proportional to a real expression whose zeros can be easily predicted, as in the previous case. In particular, a real zero always occurs between two consecutive modes of same  $\sigma_n$ . Moreover, there is an odd number of real zeros below the lowest mode, when  $i\sigma_1 \beta = -1$ , and an even (or zero) number when  $i\sigma_1 \beta = 1$ , with a similar result above the highest mode but for opposite signs of  $i\sigma_N \beta$ . This is simply illustrated in Figs. 4(b,c).

For ISFs ( $\beta = \pm 1$ ), in this case inverse Chebyshev or elliptic of even order  $N$  ( $\gamma = -1$ ), with a total of  $N/2$  positive-frequency transmission zeros on each side of the passband, it is necessary to have

$$\sigma_n = \frac{1}{\beta} (-1)^{n-1} i^{N-1}; \quad \beta = \frac{C_{11} C_{21}^*}{|C_{11} C_{21}|}. \quad (24)$$

**Case (c)**  $0 < |C_{11}| \ll |C_{21}| < 1$ : This is a band-stop filter with finite small reflection at  $\omega \rightarrow \infty$ . Similar analysis by considering  $S_{11}$  dictates, for even-order inverse Chebyshev or elliptic ISFs,

$$\sigma_n = \frac{1}{\beta} (-1)^{n-1} i^{N+1}; \quad \beta = \frac{C_{11} C_{21}^*}{|C_{11} C_{21}|}. \quad (25)$$

**Case (d)**  $C_{11} = 0 \Leftrightarrow |C_{21}| = 1$ : This is a band-stop filter with zero reflection at  $\omega \rightarrow \infty$  and a ISF implementation requires again simply

$$\sigma_n = \pm \sqrt{\gamma} (-1)^{n-1}. \quad (26)$$

By designing  $\sigma_n$  to satisfy the appropriate condition from Eqs. (23–26) according to the filter type, the pole residues in the partial-fraction expansion of  $H(\omega)$  are also matched and thus the filter design is complete.

*Approximate solutions*— Negative-frequency modes are necessary to exactly satisfy realness. However, for filters with high- $Q$  modes, the response can be well approximated (at positive frequencies  $\omega$ ) by the well-known rotating-wave approximation (RWA) of including only positive-frequency modes in QNMT. In this case, the previous results hold for any complex phase factor  $\gamma = e^{i\varphi}$ . Therefore, in filter design, Eqs. (23–26) permit  $\sigma_n$  to be tuned to the desired values up to an overall common phase factor (expressed via  $\gamma$  or  $\beta = \pm i/\sqrt{\gamma}$ ). Then, the resulting filters, even after including also negative modes with  $\sigma_n^*$  to satisfy realness, will be good approximations of ISFs within the bandwidth of interest.

As seen in Eq. (13), for  $\sigma = \pm 1$  ( $\gamma = 1$ ),  $S$  computed through QNMT is exactly symmetric, and it is easy to see that, for  $\sigma = \pm i$  ( $\gamma = -1$ ),  $S = \bar{S}C$  is also symmetric with  $C_{22} = -C_{11}$ . However, when  $\gamma$  is complex, the reciprocity condition Eq. (16) cannot be satisfied with a constant  $C$ . Since an actual physical system is obviously

reciprocal, even when designed for complex  $\gamma$ , this means that  $C$  is necessarily non-constant, but rather slowly varying due to other modes, in a way that guarantees reciprocity (note [63]). Therefore, for design purposes, once the optimized structure has been obtained, there is no need for further fine-tuning optimization. Now, if one also cares to obtain a more precise QNMT description of this structure, the procedure of Section II (including all modes and fine-tuning  $D$ 's) can be followed.

*Geometrical symmetry*—  $\sigma_n = \pm 1$  means that the radiative part of the modes is even or odd, which can be easily obtained using a structure with geometrical (e.g. mirror) symmetry between the two ports [50]. This can explain the increase in transmission previously observed in symmetric structures [64]. However, we will later see filter designs where it is preferable for the structure to *not* be symmetric, so the modes themselves are not even or odd, even though their radiative far fields may in fact be (satisfying  $\sigma_n = \pm 1$ ).

On the other hand, for  $\gamma \neq 1$ , the mode and structure have to be asymmetric anyway. In particular, even-order antimetric ISFs ( $\gamma = -1$ ) can be made only from asymmetric structures, as confirmed for example by their known corresponding electric-circuit topologies [1]. However, we explained that good approximate filters can be obtained with  $\gamma$  deviating from its optimal value by a phase factor (as long as the background  $C$  is slowly varying, in contrast to being constant for ISFs). Therefore, approximate even-order ISFs can be designed also with  $\gamma = 1$ . To highlight this point, we later show implementations of such filters, using *symmetric* structures.

*Summary*— A  $N$ -order 2-port filter, whose reflection is zero at  $N$  real frequencies, obeys  $S_{22} = \gamma S_{11}$  ( $\gamma = \pm 1$ ) and consists only of modes whose radiation couples to the two ports with the ratios  $\sigma_n = \pm \sqrt{\gamma}$ . To design standard filters, these ratios must alternate sign among consecutive modes, and a background scattering  $C$ , appropriate for the desired filter type, must be established [Eqs. (23–26)]. Approximate filters can also be designed with complex unitary  $\gamma$ . Once the QNMT design objectives (background transmission  $|C_{21}|$ , eigenfrequencies  $\omega_n$  and port-coupling ratios  $\sigma_n$ ) have been determined for the desired filter profile, the physical metasurface parameters can be identified using adequate optimization/nonlinear-solver tools.

#### IV. MICROWAVE METASURFACES

As an example of application of our theory, we design microwave frequency selective surfaces (FSS), which are usually used to implement spatial (wave) filters for communication antennas, radars, radomes [10–12], lenses [65, 66] etc. FSSs typically take the form of two-dimensional periodic metal-dielectric arrays exhibiting specific frequency-dependent transmission or reflection under planewave excitation. While older designs

were based on wavelength-sized unit cells (as in typical antenna design), the use of subwavelength dimensions to form metasurfaces has attracted much attention in the past decade due to multiple advantages, such as higher unit-cells density and smaller angular sensitivity [26, 27, 67]. An important design challenge in frequency-selective metasurfaces is the ability to obtain specific high-order frequency responses using their strongly inter-coupled subwavelength resonances, attempted usually through multilayer FSSs. As mentioned in the introduction, a very common design method uses equivalent circuit models [26–31]. The basic FSS building blocks are metallic patches with gaps (effective capacitors  $C$ ) and apertures/loops (effective inductors  $L$ ) that can be combined to make effective  $LC$  resonators. Then, the shape, size and arrangement of patches and apertures in the FSS dielectric and metallic sheets are designed to accomplish the necessary circuit topology and element-values for the transmission desired. While such circuit models can give a good physical intuition about the expected response of a FSS and can therefore be very useful to choose an appropriate topology for the desired functionality, they are too approximate and less flexible for a precise design method. This is why, although particular attention has been given to the design of elliptic filters, most of previous efforts have only achieved a very approximate “quasi-elliptic” profile response [21–25].

The QNMT we have presented in this article gives a direct pathway to precisely design high-order metasurface filters. In this section, we obtain all types of bandpass and bandstop ISFs with different orders and bandwidths. For each desired filter, we choose a fixed topology, based on these circuit-theory principles and also on intuition from QNMT itself (for the background scattering  $C$ ), with few unknown physical parameters. These are optimally identified by simply applying a multivariable solver of nonlinear systems of equations on the filter conditions derived in section III. This rather “traditional” approach leads to very rapid computational design, as physics and analytics have already been used to facilitate the job of the optimizer.

### A. Second-order bandpass filter - Circuit model

We start by studying a simple *symmetric* second-order metasurface, in order to build some physical intuition on how a particular structural topology can be modeled by an effective circuit, to relate this circuit to the QNMT, and to derive design guidelines for transmission-zero placement. The metasurface, shown in Fig. 5(a), is formed by two planar metallic sheets sandwiched between three uniform dielectric layers. A square array (with period  $a$ ) of narrow cross-like apertures in each metallic sheet creates a resonance, which can be modeled in the subwavelength limit ( $a \ll \lambda$ ) as an effective shunt parallel  $L_a C_a$  ( $\equiv 1/\omega_a^2$ ) to a plane wave incoming from free space with impedance  $Z$ . The inductance  $L_a$  originates

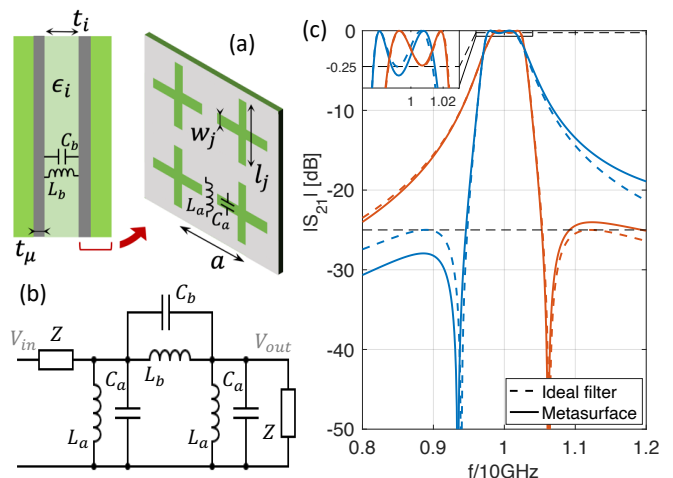


FIG. 5. (a) Symmetric metasurface for a second-order bandpass filter centered at 10 GHz with a single transmission-zero, designed for 0.25 dB passband ripple and 25 dB stopband attenuation (black dashed lines). (b) Equivalent circuit model. The coupling  $L_b C_b$  gives the transmission-zero. (c) Transmission spectrum of two optimized structures with a zero respectively on the left (L) and on the right (R) of their transmission peaks. Parameters for structure (L):  $a = 6\text{mm}$ ,  $w_1/a = w_2/a = 0.0479$ ,  $l_1/a = l_2/a = 0.846$ ,  $t_1/a = t_3/a = 0.493$ ,  $t_2/a = 0.257$ ,  $\epsilon_1 = \epsilon_3 = 1.43$ ,  $\epsilon_2 = 14.51$ . Parameters for structure (R):  $a = 9.34\text{mm}$ ,  $w_1/a = w_2/a = 0.00877$ ,  $l_1/a = l_2/a = 0.905$ ,  $t_1/a = t_3/a = 0.0237$ ,  $t_2/a = 0.0966$ ,  $\epsilon_1 = \epsilon_3 = 4.12$ ,  $\epsilon_2 = 3.80$ .

from the current flowing around the edge of the aperture, while the capacitance  $C_a$  comes from the opposite-charge accumulation across facing sides of this narrow gap [see Fig. 5(a)]. The connected topology of the metallic sheets represents a short-circuit to an incident plane wave at long wavelengths (shunt  $L_a$ ), leading to no transmission at zero frequency. Moreover, a longitudinal inductance  $L_b$  couples the apertures on the two metallic sheets, corresponding both to first-order transmission-line effects of the thin dielectric layer and to the direct mutual inductance between the apertures (which, we remind, are always centered and facing each other). Finally, capacitance  $C_b$  builds up between the two metallic sheets [see Fig. 5(a)], which is an interesting feature that has an important consequence: it leads to the emergence, in series with the path of incident-wave propagation (longitudinally), of a parallel-resonant  $L_b C_b$ , which becomes an open circuit at the frequency  $\omega_b = 1/\sqrt{L_b C_b}$ , thus leading to a zero in the transmission function. The final equivalent-circuit model is given in Fig. 5(b), corresponding to a passband filter with a finite-frequency zero.

The transmission spectrum can be computed through  $S_{21} = 2V_{out}/V_{in}$  [1], and with  $y_j = Z(1/\omega L_j - \omega C_j)$  for  $j = a, b$  we obtain:

$$S_{21}(\omega) = \frac{2iy_b}{(1 + iy_a)(1 + i(y_a + 2y_b))}. \quad (27)$$

This clearly shows transmission zeros at  $\pm\omega_b$ , and also at

$\omega = 0$ ,  $\omega \rightarrow \infty$  (bandpass behavior). Denoting the loss rates  $\Gamma_j = 1/(2ZC_j)$ , the denominator shows the system poles at  $\pm\Omega_1 - i\Gamma_1$  and  $\pm\Omega_2 - i\Gamma_2$ , where  $\Gamma_1 = \Gamma_a$ ,  $\Omega_1 \approx \omega_a$ ,  $\Gamma_2 = 1/(1/\Gamma_a + 2/\Gamma_b)$ ,  $\Omega_2 \approx \Gamma_2(\omega_a/\Gamma_a + 2\omega_b/\Gamma_b)$ . One system resonance is identical to the single-sheet resonance, while the second is affected also by the inter-sheet couplings: it is always narrower ( $\Gamma_2 < \Gamma_1$ ) and  $\Omega_2 \gtrless \Omega_1$  if  $\omega_b \gtrless \omega_a$ .

When  $\omega$  is close to the positive resonances, the RWA  $y_j \approx (\omega_j - \omega)/\Gamma_j$  effectively drops the negative resonances. Then, a partial-fraction expansion of Eq. (27) can be obtained:

$$S_{21}(\omega) \approx \frac{i\Gamma_1}{\omega - (\Omega_1 - i\Gamma_1)} - \frac{i\Gamma_2}{\omega - (\Omega_2 - i\Gamma_2)}, \quad (28)$$

This is identical to QNMT result in Eq. (D3) with  $\sigma = (-1, 1)$ . As mentioned earlier, the two *different* values for the decay rate  $\Gamma$  lead to a transmission zero, which is not usually described in typical CMT models that assume equal  $\Gamma$  for the two resonances.

We saw from Eq. (22) that this zero  $\omega_b$  appears on the side of the resonance with the smallest loss rate, which is  $\Gamma_2$  in this case, so  $\omega_b < \Omega_2 < \Omega_1 = \omega_a \Leftrightarrow L_a C_a < L_b C_b$  or the opposite order. Therefore, we have a recipe to design the zero for this metasurface, based on the equivalent circuit elements. To translate those to physical structural parameters, we observe that, in the quasi-static limit,  $L_b \propto t_2$  (see Appendix G) and  $C_b \propto \epsilon_2/t_2$ , where  $t_2$  is the small separation between the two metallic sheets and  $\epsilon_2$  is the dielectric constant of the separating layer. This means that  $L_b C_b \propto \epsilon_2$  and does not depend on  $t_2$  to first order. On the other hand,  $L_a C_a$  also does not depend on  $t_2$ , but it has a weighted dependence on  $\epsilon_1$  and  $\epsilon_2$ . The location of the transmission zero relative to the poles then mainly depends on the ratio of permittivities of the two dielectric materials. In particular, a zero at a frequency below the poles is obtained using a large  $\epsilon_2/\epsilon_1 > 1$ .

We can also use Eq. (28) to compute the full-transmission frequencies ( $|S_{21}(\omega_t)| = 1$ ):

$$\omega_t = \frac{\Omega_1 + \Omega_2}{2} \pm \sqrt{\left(\frac{\Omega_1 - \Omega_2}{2}\right)^2 - \Gamma_1 \Gamma_2}. \quad (29)$$

We see that there are two full-transmission maxima between  $\Omega_1$  and  $\Omega_2$ , as long as the eigenfrequencies are well separated ( $|\Omega_1 - \Omega_2| > 2\sqrt{\Gamma_1 \Gamma_2}$ ).

We can now use the QNMT to design second-order bandpass filters with a transmission-zero either on the right or on the left of the transmission peaks. In both cases, we choose the two complex eigenfrequencies, for which Eq. (28) gives a transmission peak-to-peak passband ripple of 0.25 dB, a stopband attenuation of at least 25 dB and a 3dB-bandwidth of 5% around the center frequency  $f_c = 10$  GHz. (For comparison, we will target these passband/stopband limits and center frequency for all filters designed in this article.) Then, we use the multivariable nonlinear-equation solver to find the structural

parameters that will make the eigenmodes of the metasurface of Fig. 5(a) match those desired eigenfrequencies and with port-coupling ratios  $\sigma = \pm(1, -1)$ . Results for optimized structures are shown in Fig. 5(c). We note that, as expected, the structure with a transmission-zero at smaller frequencies has a larger dielectric constant for the inside layer. We also see that the shapes of the transmission spectra deviate somewhat from the ideal filters. This is mainly due to higher-frequency resonances that affect the scattering matrix (acting as a background  $C$ ) and make it different from the two-poles approximation of Eq. (28), leading to slight reduction of transmission at low frequencies and increase at higher ones. As commonly known for metasurfaces, higher-order diffraction modes can be pushed away by looking, if possible, for solutions with reduced periodicity  $a$  and higher permittivities  $\epsilon_j$ .

## B. Third-order bandpass filters

Using the QNMT design method, as well as guidance from the previous two-pole bandpass structure, we now design all four standard types mentioned in section III for third-order bandpass filters. The three poles necessary for each wanted filter are given by standard analytical expressions or software tools [1]. Since all filter types are of third order with  $C_{21} = 0$  [case (a)], we see from Eq. (23) that we trivially need port-coupling coefficients  $D$  with ratios  $\sigma \propto (1, -1, 1)$  for the three modes.

To implement these filters, we use a structure with the same unit-cell topology as in Fig. 5(a), but with three metallic sheets and four dielectric layers. Based on the insight gained in section IV A from the effective circuit model, we realize that each of the inside layers will create a longitudinal parallel  $L_j C_j \propto \epsilon_j$  resonance, which will cause a transmission zero  $\propto 1/\sqrt{\epsilon_j}$ . For the inverse Chebyshev and elliptic filters, two *distinct* zeros are required. Therefore, we need different dielectric constants  $\epsilon_j$  for the inside layers. This means that the physical structure for these filter types must *not* be symmetric, so their modes are not even or odd, even if their radiative tails are [ $\sigma = (1, -1, 1)$ ]. On the other hand, Butterworth and Chebyshev filters do not have real zeros, so there we can choose a symmetric structure, which simplifies the optimization problem, as only eigenfrequencies need to be matched (in the correct order of modal symmetry). However, for these “zeroless” ISFs, the challenge with the chosen metasurface topology is to push away from our bandwidth the unavoidable zero that will arise from the inside layers. The simplest way to accomplish this, is to look for solutions where these layers are thick enough that the second-order dependence of the longitudinal parallel  $L_j C_j$  on  $t_j$  moves the zero to sufficiently high frequencies. Different topologies could also be devised that eliminate either the mutual inductance or capacitance between sheets.

Again by optimizing the structural topology, for each

filter, we get the desired three complex resonant frequencies  $\omega_n$  and their corresponding  $\sigma_n$ . Transmissions of the optimized metasurfaces that implement the four filter types with  $\sim 5\text{-}6\%$  3dB-bandwidth are shown in Fig. 6(a), while in Fig. 6(b) only for elliptic filters with varying bandwidth ( $\sim 2\text{-}10\%$ ). We note a good agreement with the ideal filters, except for small discrepancies again due to effects from higher-order modes and to small errors in the values of optimized resonances. Notice that, indeed, Butterworth and Chebyshev filters require thick inside dielectric layers to move the zero away and that smaller bandwidths need higher  $\epsilon_j$  to increase the modal  $Q$ s. Moreover, we test once more the effect of metal (here, copper) losses on an elliptic filter and find again that it mainly just reduces the values of the transmission peaks (only by  $\sim 0.5$  dB at 10 GHz operation).

### C. Third-order elliptic bandstop filter

In order to design a third-order *bandstop* filter, we now need to achieve a full-transmission background  $|C_{21}| = 1$  [case (d)], and then Eq. (26) dictates again three QNMs with  $\sigma \propto (1, -1, 1)$ . As explained in detail in section II, the background- $C$  design can generally be understood using the system low- $Q$  modes and, in particular, we show in Appendix F that a fully-transmissive  $C$  can be achieved by a mode with infinite radiative rate, which effectively models free space. Thus, as expected, we need a physical structure with a very small effective index ( $\sim 1$ ), while still able to support the required high- $Q$  resonances. Moreover, since we want full transmission at zero frequency, the metallic components now should not have a fully-connected topology. Therefore, relying on the principle of duality, we choose, in place of each metallic sheet with cross apertures, an array of non-connected thin metallic crosses (as in Fig. 2). These are supported by dielectric crosses, also non-connected to minimize the total effective index. The structure is shown as an inset in Fig. 7(a). Its effective circuit model now sees each array of crosses as a shunt series- $LC$  resonance, where  $L$  is the inductance of the cross wires and  $C$  is the capacitance across adjacent crosses within each array [see Fig. 7(a)], and then the couplings between arrays are effectively longitudinal parallel- $LC$ , where  $C$  is the capacitance across facing (cocentric) crosses and  $L$  is the first-order transmission-line model of propagation through the free space, but also includes the small contribution (a large in-parallel value, see Appendix G) of the mutual inductance between facing crosses. This circuit can implement the desired ISF, where each shunt series- $LC$  or longitudinal parallel- $LC$  can directly impose one of the required three distinct transmission zeros.

An example of an optimized structure with a third-order elliptic bandstop response of 12% 3dB-bandwidth is shown in Fig. 7(a). We note again the very good agreement compared to the ideal filter. Notice that, in duality to the passband filter, the permittivity of one inside di-

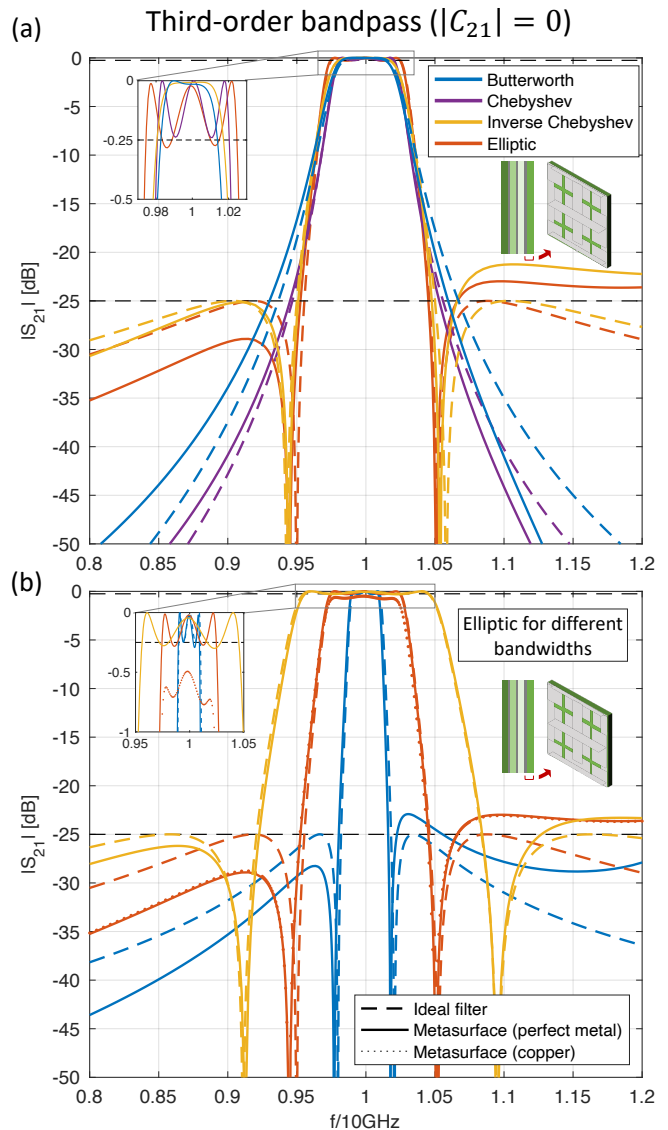


FIG. 6. Optimized third-order bandpass filters (a) of different types with same bandwidth and (b) elliptic only for different bandwidths. We use the same structure as in Fig. 5 but with three metallic sheets and four dielectric layers. Physical parameters are provided in Appendix H. We notice good agreement of lossless structures (solid lines) with ideal filters (dashed lines), except for small deviations mainly due to effects from high-order modes. Copper losses (dotted line) reduce peak transmission while preserving the filter’s shape.

electric turns out to be *smaller* than the outside layers.

### D. Second-order elliptic bandpass and bandstop filters

To complete our set of design examples, we now demonstrate second-order elliptic bandpass and bandstop metasurface filters. In this case, we need to design a specific non-trivial background  $C$ , in particular,

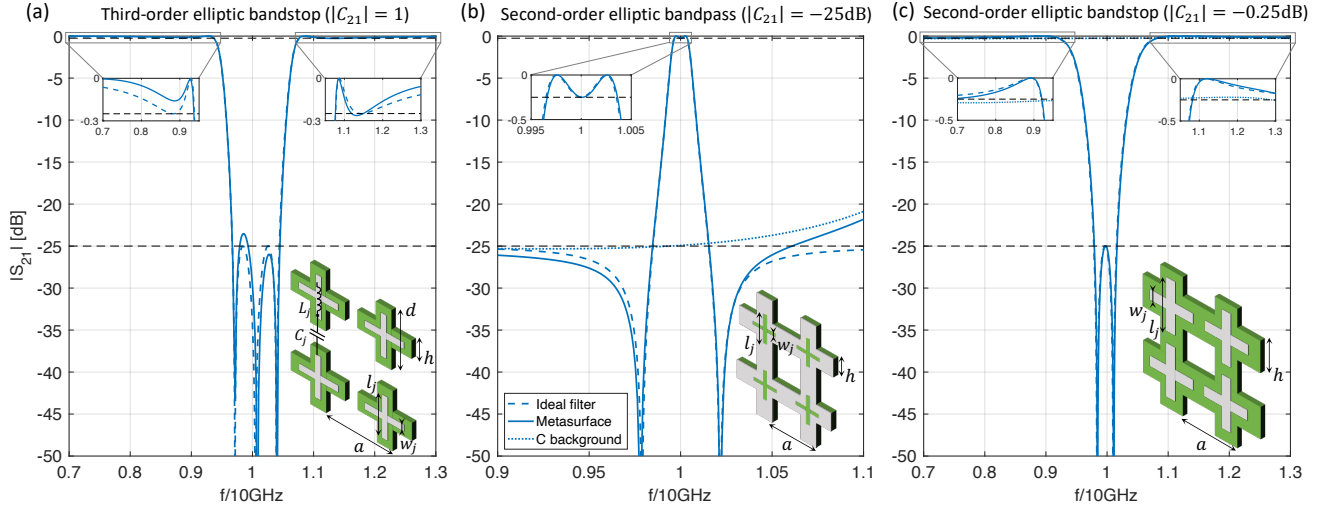


FIG. 7. (a) Third-order elliptic bandstop filter. The structure has three metallic-cross arrays and four dielectric layers with parameters:  $a = 16.99\text{mm}$ ,  $h/a = 0.03$ ,  $d/a = 0.619$ ,  $w/a = (1.53, 3.73, 1.61) \times 10^{-3}$ ,  $l/a = (0.558, 0.589, 0.524)$ ,  $t/a = (0.166, 0.358, 0.441, 0.183)$ ,  $\epsilon = (4.76, 3.22, 4.05, 4.50)$ . (b) Second-order elliptic bandpass filter. The structure has two metallic sheets and three dielectric layers with parameters:  $a = 17.571\text{mm}$ ,  $h/a = 0.456$ ,  $w_1/a = w_2/a = 6.08 \times 10^{-3}$ ,  $l_1/a = l_2/a = 0.4355$ ,  $t_1/a = t_3/a = 0.3072$ ,  $t_2/a = 0.3169$ ,  $\epsilon_1 = \epsilon_3 = 3.82$ ,  $\epsilon_2 = 1.893$ . (c) Second-order elliptic bandstop filter. The structure has two metallic-cross arrays and three dielectric layers with parameters:  $a = 18.70\text{mm}$ ,  $h/a = 0.181$ ,  $w_1/a = w_2/a = 2.74 \times 10^{-3}$ ,  $l_1/a = l_2/a = 0.514$ ,  $t_1/a = t_3/a = 0.204$ ,  $t_2/a = 0.332$ ,  $\epsilon_1 = \epsilon_3 = 1.60$ ,  $\epsilon_2 = 3.10$ . All filters satisfy quite well the marked requirements (black dashed lines) and agree with the ideal filters.

$C_{21}$  must be roughly constant within the bandwidth of interest and its amplitude set respectively to the desired stopband minimum attenuation value ( $-25$  dB) [case (b)] or passband maximum ripple value ( $-0.25$  dB) [case (c)]. Furthermore, the coefficients  $\sigma_n$  should respectively satisfy Eq. (24) or Eq. (25). As discussed in section III, for even-order ISFs,  $\gamma = -1$  and  $C$  is a real constant matrix, so  $\beta \equiv C_{11}C_{21}^*/|C_{11}C_{21}| = \pm 1$  and  $\sigma_n = \pm i$ , which corresponds to asymmetric structures, such as the standard circuit topologies of even-order ISFs. However, we explained that approximate solutions with a different unitary  $\gamma$  are possible (using the RWA) and here we present *symmetric* structures ( $\gamma = 1$ ) exhibiting a second-order elliptic filter response within the bandwidth of interest. Since symmetry guarantees  $\sigma_n = \pm 1$ , Eqs. (24,25) become design objectives for  $\beta$ , which must respectively match  $\pm i/\sigma_1$ .

For the bandpass filter (with two transmission zeros), we use as starting point for the structural topology that from Fig. 5(a) corresponding to a second-order bandpass filter with only one zero. There, the large metallic sheets led to  $C_{21} = 0$ . In order to increase  $|C_{21}|$  to the small required  $-25$  dB around the filter center-frequency  $\omega_c$ , we open holes through the entire metasurface, as shown in Fig. 7(b), so that some of the incident wave will directly go through without coupling to the high- $Q$  resonances of the crosses. Excluding those two high- $Q$  modes, we calculate  $C$  using QNMT, and it turns out that even-odd pairs of *almost* degenerate low- $Q$  modes below  $\omega_c$  together with higher-order modes lead to a background with a flat small  $|C_{21}|$  and constant  $\beta$  over a fairly large fre-

quency range (see modes in Supplemental Material [47]). [Traditionally, one would approximate  $C$  by simulating an effective background structure (e.g. where the cross apertures which cause the high- $Q$  resonances are closed), but the result is inaccurate ( $-19$  dB instead of  $-25$  dB).] The optimization then consists of enforcing the values of the two complex eigenfrequencies,  $|C_{21}(\omega_c)| = -25$  dB and, from Eq. (24),  $\beta(\omega_c) = i/\sigma_1$ . The transmission of the designed structure is shown in Fig. 7(b) and agrees very well with the 1%-bandwidth ISF spectrum. It turns out that the modal symmetry is  $\sigma = (-1, 1)$ , so  $\beta(\omega_c) = -i$ . Note that, since each metallic sheet is still connected (in a topological sense), the transmission at very long wavelengths will still go to zero.

For the second-order bandstop elliptic filter, we use as starting point the structural topology from Fig. 7(a) for the third-order bandstop filter, but with two metallic-cross arrays sandwiched between three dielectric layers. There, the effective refractive index of the entire metasurface was designed small to get  $|C_{21}(\omega_c)| \approx 1$ . In order to decrease  $|C_{21}|$  to the required  $-0.25$  dB, we connect the dielectric crosses, as shown in Fig. 7(c), to reflect back some of the incident wave. In QNMT terms, an averaging over the metasurface leads to an effective slab of low refractive index, which supports equispaced “Fabry-Perot” low- $Q$  modes  $\omega_n^C$  (see Appendix F); the “Fabry-Perot” transmission hits  $|C_{21}| = 1$  at  $\Omega_n^C$ , but is less than 1 and flat between modes ( $\omega_n^C, \omega_{n+1}^C$ ), with roughly constant  $\beta \approx i$  if  $n$  even (and  $\beta \approx -i$  if  $n$  odd). For this structure, it turns out that these modes  $\omega_n^C$  have such a small  $Q$  (see modes in Supplemental Material [47])

that it is difficult to accurately find all of those contributing to  $C(\omega_c)$ . Therefore, we instead calculate it indirectly from  $C(\omega_c) = \bar{S}^{-1}(\omega_c)S(\omega_c)$ , as explained earlier. [Again, the traditional method of an effective background structure (removing the metallic crosses) gives a noticeably less accurate estimate of  $C$  ( $-0.11$  dB instead of  $-0.25$  dB).] The two high- $Q$  modes have symmetry  $\sigma = (-1, 1)$ , consistent with  $\beta(\omega_c) = i$  from Eq. (25), and the optimized final structure has transmission shown in Fig. 7(c), matching precisely an elliptic bandstop ISF of 10% bandwidth.

### E. Fabrication and tunability

All the metasurface filters that we presented were based on a layered topology with metallic sheets sandwiched between dielectric layers. This layered form was chosen, because it has the great advantage of allowing easy fabrication. Especially in the cases where patterning is only on the metallic sheets, these metasurfaces can be manufactured even with widespread printed-circuit board (pcb) techniques. In fact, all designed ISFs presented in this article used dielectrics with permittivities less than 11.2, which is roughly the upper limit for (typically  $\text{Al}_2\text{O}_3$ -based) low-loss materials compatible with pcbs. Furthermore, the clear separation between metallic sheets allows them to be connected to separate electrodes, where voltage can be applied to potentially tune the permittivity of the intermediate dielectrics, if those are chosen to be tunable materials (liquid crystals, ferroelectrics etc.) [68]. Previous attempts at elliptic filters have usually employed topologies with shunt metal paths connecting different metal sections within the metasurface, which hinders both these benefits [22–24].

## V. CONCLUSIONS

We have presented a systematic method using eigen-solvers for designing standard filters or other useful transmission/reflection spectra, especially ones with multiple finite real zeros, allowing ultra-compact devices with spatially overlapping resonances (unlike previous circuit-theory or CMT approaches). It is based on a non-normalized QNM expansion of the system scattering matrix  $S$ , formulated to satisfy the physical conditions of realness, energy conservation and reciprocity. It entails identifying the necessary background response  $C$ , the exact complex eigenfrequencies  $\omega_n$  of these modes, and the values of the ratios  $\sigma_{r,pn}$  with which these modes must couple to the system coupling ports, to achieve the desired scattering frequency profile. An efficient optimization procedure is then applied to determine the structural parameters (geometry and materials) that meet these criteria. We have demonstrated the method for microwave planar metasurface filters, for all standard amplitude-filter types (especially the most challenging, elliptic), for

both bandpass and bandstop behaviors, and for a variety of frequency bandwidths.

In our examples, we used fixed topologies, guided by general physical intuition from circuit models, and then applied a simple multi-variable equation solver to obtain a small set of structural parameters. In principle, our conditions can also be combined with various large-scale topology-optimization algorithms (where every “point” in space is a degree of freedom) and solver methods [44]. While we focused on amplitude standard filters, our design process can be used for any desired scattering spectrum, by fitting it to QNMT to extract the corresponding eigenmode optimization objectives  $(\omega_n, \sigma_{r,pn})$ . Moreover, it should be clear that the accurate QNMT prediction of the time delay also makes the theory applicable to design phase filters, such as all-pass delay filters [69] (useful also for metalenses [70]). Our design method was demonstrated for microwave metasurfaces, but it can also be used for resonant systems with any qualitatively similar physics, such as mechanical, acoustic, photonic, or quantum-electronic filters.

Our QNMT was mainly developed for linear ports with frequency-independent transverse mode profiles, such as plane waves. However, it could also be extended to finite arbitrary-shape scatterers using a spherical CPM basis. (Note that systems with spherical symmetry studied in previous QNMT formulations [36, 37] can be modeled merely as multiple 1-ports, so knowledge of only the poles is sufficient [71] and QNMT was not really needed.) Difficulties arise with other types of ports, such as when QNM-to-CPM coupling coefficients  $D(\omega)$  are frequency dependent, and specifically when the  $S$  matrix has branch points due to CPM cutoff frequencies. While a rigorous extension of the theory to such systems may require a different approach, our model may still provide good approximate results for slowly varying coupling coefficients (such as for dielectric waveguides with low waveguide dispersion).

## ACKNOWLEDGMENTS

This work was supported in part by the U.S. Army Research Office through the Institute for Soldier Nanotechnologies at MIT under award W911NF-18-2-0048, by the Simons Foundation collaboration on Extreme Wave Phenomena, and by Lockheed Martin Corporation under award RPP2016-005.

### Appendix A: Weierstrass factorization of $S$ -matrix

The Weierstrass factorization theorem [72] states that a “meromorphic” function (analytic except for poles) can be factorized into a non-zero analytic function (an exponential) and a rational function (zeros and poles). If  $S(\omega)$  is meromorphic, an exponential phase factor can then be factored out of each term as  $S_{pq}(\omega) = e^{i\varphi_{pq}(\omega)} S'_{pq}(\omega)$ ,

with  $S'_{pq}$  a ‘‘proper’’ rational function (degree of numerator polynomial not larger than degree of denominator, so finite as  $\omega \rightarrow \infty$ ) and  $\varphi_{pq}$  an analytic function that we assume corresponds to a real phase shift for real frequencies. Similarly to the approach in Ref. 71, the combination of Phragmén-Lindelöf theorem (giving  $|e^{i\varphi_{pq}(\omega)}| \leq 1$  in the upper-half complex plane) and Čebotarev theorem shows that  $\varphi_{pq}$  has to be a linear ( $= \tau_{pq}\omega$  with  $\tau_{pq} \geq 0$ , since the constant term can be added to  $S'_{pq}$ ).

When the system is lossless and reciprocal, unitarity and symmetry of  $S$  combine to  $S^*(\omega)S(\omega) = I$ . The off-diagonal  $pq$  term can be expanded as  $\sum_r S_{pr}^* S_{rq} = \sum_r e^{-i(\tau_{pr} - \tau_{rq})\omega} S_{pr}^* S'_{rq} = 0$ . Since this has to be true for all real  $\omega$ , all the phase terms in the sum must be the same, namely  $\tau_{pr} - \tau_{rq} = \theta_{pq}$  for each  $r$ . Specifically, for  $r = p$  and  $r = q$ , we get  $\tau_{pp} - \tau_{pq} = \tau_{pq} - \tau_{qq} \Leftrightarrow \tau_{pq} = (\tau_{pp} + \tau_{qq})/2$ . Therefore, the  $S$  matrix can be written as  $S = e^{i\tau\omega} S' e^{i\tau\omega}$  with a *diagonal*  $\tau$  matrix with real positive elements.

### Appendix B: Energy conservation condition Eq. (6)

For a lossless system,  $S$  is unitary. From Eq. (5), namely  $S = I - DdK^t$ , where  $d = (i\omega - i\Omega)^{-1}$ :

$$S^\dagger S = I - K^* d^\dagger D^\dagger - DdK^t + K^* d^\dagger D^\dagger DdK^t. \quad (\text{B1})$$

We compute the coefficient  $(p, q)$  of this matrix. The second and third terms are equal to:

$$\sum_n \frac{K_{pn}^* D_{qn}^*}{i(\omega - \omega_n^*)} - \sum_n \frac{D_{pn} K_{qn}}{i(\omega - \omega_n)}. \quad (\text{B2})$$

The final term, after decomposing into simple elements through  $\frac{1}{i(\omega - \omega_n)i(\omega - \omega_l^*)} = \frac{1}{i(\omega_n - \omega_l^*)} \left[ \frac{1}{i(\omega - \omega_n)} - \frac{1}{i(\omega - \omega_l^*)} \right]$  and relabelling indices ( $n$  and  $l$ ), becomes:

$$\begin{aligned} & \sum_{r,n,l} \frac{K_{pl}^* D_{rl}^* D_{rn} K_{qn}}{i(\omega - \omega_l^*)i(\omega - \omega_n)} = \\ & = \sum_n \frac{K_{qn}}{i(\omega - \omega_n)} \sum_l K_{pl}^* \sum_r \frac{D_{rn} D_{rl}^*}{i(\omega_n - \omega_l^*)} \\ & - \sum_n \frac{K_{pn}^*}{i(\omega - \omega_n^*)} \sum_l K_{ql} \frac{\sum_r D_{rl} D_{rn}^*}{i(\omega_l - \omega_n^*)}. \end{aligned} \quad (\text{B3})$$

In order to impose  $S^\dagger S = I$  for every  $\omega$ , necessary and sufficient conditions are given by  $K^* M = -D$  and  $K M^t = -D^*$ , with  $M_{nl} = \frac{\sum_p D_{pl} D_{pn}^*}{i(\omega_l - \omega_n^*)}$ . The two relations are actually equivalent, since  $M = M^\dagger$ , and can be rewritten as  $K^t = -M^{-1} D^\dagger$ .

### Appendix C: Realness under Eq. (6)

Including negative-frequency modes with  $D_{pn'} = D_{pn}^*$ , we can write  $M = \begin{pmatrix} A & B \\ B^* & A^* \end{pmatrix}$  (where  $A = A^\dagger$  and

$B = B^t$ , so that  $M = M^\dagger$ ). Now, consider matrices  $\tilde{A}$ ,  $\tilde{B}$  such that  $(\tilde{A} \ \tilde{B}) M = (I \ 0)$ ; then, by directly substituting  $M$ , we can immediately show that we also have  $(\tilde{B}^* \ \tilde{A}^*) M = (0 \ I)$ , so  $M^{-1} = \begin{pmatrix} \tilde{A} & \tilde{B} \\ \tilde{B}^* & \tilde{A}^* \end{pmatrix}$ . Finally, from  $K = -D^* (M^t)^{-1}$ , we conclude that  $K_{pn'} = K_{pn}^*$ .

### Appendix D: Normalization independence of Eq.(7)

Let  $D_r$  be a  $N \times N$  diagonal matrix, with elements  $D_{r,nn} = D_{r_n n}$ , for some chosen port  $r_n$  for each resonant mode  $n$  (usually, we simply take  $r_n = 1$ ). Then, denote by  $\sigma_r = D D_r^{-1}$  the  $r$ -scaled  $P \times N$  coupling matrix (naturally,  $\sigma_{r,r_n n} = 1$  for all  $n$ ). Now, by inserting  $I$  twice in Eq. (7), the scattering matrix  $S$  from can be rewritten as

$$\begin{aligned} S &= I + D(i\omega - i\Omega)^{-1} M^{-1} D^\dagger \\ &= I + D (D_r^{-1} D_r) (i\omega - i\Omega)^{-1} M^{-1} \left[ D_r^\dagger (D_r^{-1})^\dagger \right] D^\dagger \\ &= I + \sigma_r (i\omega - i\Omega)^{-1} M_r^{-1} \sigma_r^\dagger, \end{aligned} \quad (\text{D1})$$

where

$$\begin{aligned} M_r &= (D_r^{-1})^\dagger M D_r^{-1} \Leftrightarrow \\ M_{r,nl} &= \frac{1}{D_{r_n n}^*} \frac{\sum_p D_{pl} D_{pn}^*}{i\omega_l - i\omega_n^*} \frac{1}{D_{rl}} = \frac{1 + \sum_{p \neq r_n} \sigma_{r,p} \sigma_{r,pn}^*}{i\omega_l - i\omega_n^*}. \end{aligned} \quad (\text{D2})$$

These two equations show that, for a lossless system,  $S$  in Eq. (7) can be fully computed using only the resonant frequencies  $\Omega$  and the ratios  $\sigma_r$  of modal coupling among different ports, independently of the overall scaling factors in  $D$ .

For 2-port systems, we simply choose  $r_n = 1$ , skip the  $r$ -subscript and denote  $\sigma_n = D_{2n}/D_{1n}$ . The  $S$ -matrix then becomes  $(p, q = 1, 2)$

$$\begin{aligned} S_{pq} &= \delta_{pq} + \sum_{n=1}^N \frac{\sigma_{pn} \sum_{l=1}^N M_{nl}^{-1} \sigma_{ql}^*}{i\omega - i\omega_n} \\ M_{nl} &= \frac{1 + \sigma_l \sigma_n^*}{i\omega_l - i\omega_n^*}; \quad \sigma_{1n} = 1, \sigma_{2n} = \sigma_n. \end{aligned} \quad (\text{D3})$$

When the system has mirror symmetry, these ratios can only take the values  $\sigma_n = \pm 1$ , so they act like eigenvalues of the symmetry operator.

Reversely, we also show that  $S$  uniquely determines  $\Omega$  and  $\sigma_r$ . In particular, for two different sets  $\{\Omega, \sigma_r\}$ ,  $\{\Omega', \sigma'_r\}$  such that  $S_{\{\Omega, \sigma_r\}} = S_{\{\Omega', \sigma'_r\}}$ , we see from Eq. (D1) that  $\Omega = \Omega'$  and

$$\sigma_{r,pn} [\sigma_r M_r^{-1}]_{qn}^* = \sigma'_{r,pn} [\sigma'_r M_r'^{-1}]_{qn}^*. \quad (\text{D4})$$

For  $p = r_n$ , we have  $[\sigma_r M_r^{-1}]_{qn} = [\sigma'_r M_r'^{-1}]_{qn}$ . Then, for any  $p$ , Eq. (D4) again gives  $\sigma_{r,pn} = \sigma'_{r,pn}$ .

### Appendix E: Properties of zeros of lossless reciprocal 2-port systems

Combining realness  $S^*(\omega) = S(-\omega)$ , unitarity  $S^\dagger(\omega)S(\omega) = I$  and symmetry  $S^t(\omega) = S(\omega)$  on the real- $\omega$  axis, gives  $S(-\omega)S(\omega) = I$ , which can then be analytically continued in the entire complex- $\omega$  plane. Expanding this equation for a 2-port, we get

$$S_{11}(-\omega)S_{11}(\omega) + S_{21}(-\omega)S_{21}(\omega) = 1 \quad (\text{E1a})$$

$$S_{11}(-\omega)S_{11}(\omega) = S_{22}(-\omega)S_{22}(\omega) \quad (\text{E1b})$$

$$S_{11}(-\omega)S_{21}(\omega) = -S_{21}(-\omega)S_{22}(\omega). \quad (\text{E1c})$$

We can use these equations to derive some useful properties of the zeros of  $S$ -coefficients. As a reminder, realness requires all poles and zeros to be symmetric across the imaginary  $\omega$ -axis.

Let's first assume that  $-\omega_o$  is *not* a system pole [so  $S(-\omega_o)$  is finite]. Eq. (E1a) then prevents  $S_{11}$  and  $S_{21} = S_{12}$  from having simultaneous zeros at  $\omega_o$ , and using also Eq. (E1b) the same holds for  $S_{22}$  and  $S_{21}$ . Therefore, Eq. (E1c) mandates that (i) the zeros of  $S_{21}$  can only appear as complex quadruplets  $(\omega_o, \omega_o^*, -\omega_o, -\omega_o^*)$ , real or imaginary pairs  $(\omega_o, -\omega_o)$ , or at  $\omega_o = 0$  and that (ii), for each zero-pair  $(\omega_o, -\omega_o^*)$  of  $S_{11}$ ,  $(-\omega_o, \omega_o^*)$  is a zero-pair of  $S_{22}$ .

If now  $-\omega_o$  is a system pole (so at least one  $S$ -element diverges there), the same rules (i) and (ii) still apply, as long as zero-pole cancellations that occur at  $(-\omega_o, \omega_o^*)$  are taken into account. All possible scenarios are: (I) If  $S_{11}(\omega_o) = 0 \neq S_{22}(\omega_o)$ , Eq. (E1b) forces  $S_{22}(-\omega_o)$  to be finite, thus  $S_{22}$  must exhibit a zero at  $-\omega_o$  that cancels the pole there (and similarly when switching  $S_{11}$  and  $S_{22}$ ). Moreover, if simultaneously  $S_{21}(\omega_o) = 0$ , Eq. (E1c) mandates a pole-zero cancellation also for  $S_{21}$  at  $-\omega_o$ . (II) If  $S_{11}(\omega_o) = S_{22}(\omega_o) = 0$ , Eq. (E1c) implies that also  $S_{21}(\omega_o) = 0$ , namely the entire matrix  $S(\omega_o) = 0$ . In this case, we can consider that all  $S$ -coefficients also have another zero at  $-\omega_o$  that cancels a degenerate pole, which usually do appear when the physical system is perturbed. (III) If  $S_{11}(\omega_o) \neq 0 \neq S_{22}(\omega_o)$ , Eq. (E1a, E1c) dictate also that  $S_{21}(\omega_o) \neq 0$ . In the cases above, for any coefficient with  $S_{pq}(\omega_o) = 0$ , then  $S_{pq}(\omega) \propto e^{i\varphi(\omega)} = (\omega - \omega_o)(\omega + \omega_o^*) / (\omega + \omega_o)(\omega - \omega_o^*)$ , a behavior known as an ‘‘all-pass’’ phase filter. Moreover, when  $S(\omega_o)$  is singular,  $\omega_o$  is called an ‘‘ $S$ -matrix zero’’ (for example generalized in Ref. 73).

The restrictions (i) on the  $S_{21}$  zeros imply that its numerator is a polynomial of  $\omega^2$  with real coefficients, optionally with multiplicative  $i\omega$  factors.

### Appendix F: Background $C$ -matrix due to an infinite- $\Gamma$ mode

Consider a 2-port system supporting a mode ( $\omega_o = \Omega_0 - i\Gamma_0$ ) with  $\Gamma_0 \rightarrow \infty$  and *real* ports-coupling ratio  $\sigma_0$ . As detailed in the main text, this mode can

be factored out of  $S$  into a unitary background response  $C$ . Using Eq. (D3) for just this mode, we find  $M_{00} = (1 + |\sigma_0|^2) / 2\Gamma_0$  and then

$$C_{pq} \rightarrow \delta_{pq} + \frac{\sigma_{p0}M_{00}^{-1}\sigma_{q0}^*}{-\Gamma_0} = \delta_{pq} - \frac{2\sigma_{p0}\sigma_{q0}^*}{1 + |\sigma_0|^2} \quad (\text{F1})$$

$$\Leftrightarrow C = \begin{pmatrix} -r & t \\ t & r \end{pmatrix}; \quad r = \frac{1 - |\sigma_0|^2}{1 + |\sigma_0|^2}, \quad t = \frac{-2\sigma_0}{1 + |\sigma_0|^2},$$

which demonstrates that the infinite  $\Gamma_0$  cancels out to give a constant background response different from  $I$ .

In particular, we get  $C = \begin{pmatrix} -1 & 0 \\ 0 & 1 \end{pmatrix}$  for  $\sigma_0 = 0$ , while

$C = \begin{pmatrix} 1 & 0 \\ 0 & -1 \end{pmatrix}$  for  $\sigma_0 \rightarrow \infty$ . For example, two such modes would appear simultaneously on the two sides of a perfect mirror (e.g. PEC), leading to the often-used  $C = -I$  [32].

A finite transmission  $t$  is achieved for  $\sigma_0 = -\frac{1}{t} \pm \sqrt{\frac{1}{t^2} - 1}$ , and specifically  $\sigma_0 = \pm 1$  gives a fully-transmissive background with  $C = \begin{pmatrix} 0 & \mp 1 \\ \mp 1 & 0 \end{pmatrix}$ .

Another way to confirm this last result is to find the modes of the simplest fully-transmissive background, free space. If we start with a uniform dielectric slab of thickness  $\tilde{t}$  and refractive index  $\tilde{n}$ , its ‘‘Fabry-Perot’’ modes are an equi-spaced spectrum given by

$$\omega_l = \frac{2c}{\tilde{n}\tilde{t}} \left( \frac{l\pi}{2} - i \cdot \text{atanh} \frac{1}{\tilde{n}} \right); \quad \sigma_l = (-1)^l. \quad (\text{F2})$$

Consider appropriately large  $\tilde{n}$ , so that  $\text{atanh}(1/\tilde{n}) \ll \pi/2 \Leftrightarrow \Gamma \ll |\Omega_{l+1} - \Omega_l|$ , and small  $\tilde{t}$ , so that only the  $l = 0$  mode has an effect at our frequencies of interest  $0 < \omega \ll \Omega_1 = c\pi/\tilde{n}\tilde{t}$ . This slab approaches free space as  $\tilde{t} \rightarrow 0$ . In this limit, all  $\Gamma_l$  and  $\Omega_{l \neq 0}$  go to infinity at the same rate (while  $\Omega_0 = 0$ ). Therefore, perhaps counter-intuitively, free space can be seen as equivalent to a mode at  $0 - i\infty$  with  $\sigma_0 = 1$ , causing full transmission.

Finally note that, interestingly, two such infinite- $\Gamma$  modes with  $\sigma = 1$  (even) and  $\sigma = -1$  (odd) do not couple and add to give full reflection with  $C = -I$ .

### Appendix G: Inductive coupling between closely-spaced apertures

For two inductors  $L_1, L_2$  with mutual inductance  $M$ , the standard T-type coupling network with elements  $L_1 - M$ ,  $L_2 - M$  and  $M$  is converted to the  $\Pi$ -type network, used in our circuit models, with element values  $(L_1L_2 - M^2) / (L_2 - M)$ ,  $(L_1L_2 - M^2) / (L_1 - M)$  and  $(L_1L_2 - M^2) / M$ . The last element represents the longitudinal inductive coupling  $L_b$  in our circuits, which becomes small for large mutual inductance  $M < \sqrt{L_1L_2}$  (and vice versa).

When  $L_1, L_2$  are aperture-type,  $M$  scales linearly with their on-axis distance  $t$  as  $M \approx M_0 - \xi t$  for  $\xi t \ll M_0$  [74],

so  $L_b \approx L_1 L_2 / M_0 - M_0 + \xi t$ . When the two apertures are not too dissimilar,  $M_0 \approx \sqrt{L_1 L_2}$ , so we finally get  $L_b \approx \xi t$  for  $M_0 (L_1 L_2 / M_0^2 - 1) \ll \xi t \ll M_0$ . Moreover treating the dielectric layer as a very short transmission line, its equivalent circuit model is also just an inductor with  $L'_b \approx \xi' t$ , where  $\xi'$  the inductance per unit length. Combining the two sources of inductance we conclude the

rough scaling  $L_b \propto t$ .

#### Appendix H: Third-order bandpass filters' structural parameters

Below are the structural parameters for the third-order bandpass filters of Fig. 6:

Type	$a$ (mm)	$w_1/a$	$w_2/a$	$w_3/a$	$l_1/a$	$l_2/a$	$l_3/a$	$t_1/a$	$t_2/a$	$t_3/a$	$t_4/a$	$\epsilon_1$	$\epsilon_2$	$\epsilon_3$	$\epsilon_4$
Butterworth	13.49	0.024	0.003	0.024	0.805	0.709	0.805	–	0.445	0.445	–	1	2.41	2.41	1
Chebyshev	12.02	0.0099	0.0027	0.0099	0.7896	0.6639	0.7896	–	0.483	0.483	–	1	3.45	3.45	1
Inverse Chebyshev	9.83	0.221	0.050	0.055	0.772	0.645	0.944	–	0.278	0.096	0.018	1	6.72	3.64	2.73
Elliptic 1	10.00	0.28	0.034	0.009	0.501	0.535	0.849	–	0.451	0.026	0.020	1	8.21	3.95	3.00
Elliptic 2	9.175	0.222	0.068	0.022	0.692	0.607	0.908	–	0.343	0.071	0.021	1	8.58	4.42	3.19
Elliptic 3	10.45	0.207	0.012	0.071	0.806	0.710	0.992	–	0.187	0.066	0.014	1	5.72	2.61	3.41

- [1] H. G. Dimopoulos, *Analog Electronic Filters: Theory, Design and Synthesis* (Springer Science & Business Media, 2011).
- [2] B. E. Little, S. T. Chu, H. A. Haus, J. Foresi, and J.-P. Laine, *Journal of Lightwave Technology* **15**, 998 (1997).
- [3] S. Fan, P. R. Villeneuve, J. D. Joannopoulos, and H. A. Haus, *Optics Express* **3**, 4 (1998).
- [4] C. Manolatou, M. Khan, S. Fan, P. R. Villeneuve, H. Haus, and J. Joannopoulos, *IEEE Journal of Quantum Electronics* **35**, 1322 (1999).
- [5] M. A. Popovic, T. Barwicz, M. R. Watts, P. T. Rakich, L. Socci, E. P. Ippen, F. X. Kärtner, and H. I. Smith, *Optics Letters* **31**, 2571 (2006).
- [6] S. Xiao, M. H. Khan, H. Shen, and M. Qi, *Optics Express* **15**, 14765 (2007).
- [7] H.-C. Liu and A. Yariv, *Optics Express* **19**, 17653 (2011).
- [8] Z. Dai, J. Wang, and Y. Heng, *Optics Express* **19**, 3667 (2011).
- [9] W. Bogaerts, P. De Heyn, T. Van Vaerenbergh, K. De Vos, S. Kumar Selvaraja, T. Claes, P. Dumon, P. Bienstman, D. Van Thourhout, and R. Baets, *Laser & Photonics Reviews* **6**, 47 (2012).
- [10] T.-K. Wu, *Frequency Selective Surface and Grid Array*, Vol. 40 (Wiley-Interscience, 1995).
- [11] J. C. Vardaxoglou, *Frequency Selective Surfaces: Analysis and Design* (Research Studies Press, 1997).
- [12] B. A. Munk, *Frequency Selective Surfaces: Theory and Design* (John Wiley & Sons, 2005).
- [13] D. Morgan, *Surface Acoustic Wave Filters: With applications to Electronic Communications and Signal Processing* (Academic Press, 2010).
- [14] A. Colombi, D. Colquitt, P. Roux, S. Guenneau, and R. V. Craster, *Scientific Reports* **6**, 1 (2016).
- [15] B. Rostami-Dogolsara, M. K. Moravvej-Farshi, and F. Nazari, *Physical Review B* **93**, 014304 (2016).
- [16] L. D'Alessandro, E. Belloni, R. Ardito, F. Braghin, and A. Corigliano, *Applied Physics Letters* **111**, 231902 (2017).
- [17] D. Colquitt, A. Colombi, R. Craster, P. Roux, and S. Guenneau, *Journal of the Mechanics and Physics of Solids* **99**, 379 (2017).
- [18] G. Manara, A. Monorchio, and R. Mittra, *Electronics Letters* **35**, 1400 (1999).
- [19] D. J. Kern, D. H. Werner, A. Monorchio, L. Lanuzza, and M. J. Wilhelm, *IEEE Transactions on Antennas and Propagation* **53**, 8 (2005).
- [20] J. A. Bossard, D. H. Werner, T. S. Mayer, J. A. Smith, Y. U. Tang, R. P. Drupp, and L. Li, *IEEE Transactions on Antennas and Propagation* **54**, 1265 (2006).
- [21] Z. H. Jiang, S. Yun, L. Lin, J. A. Bossard, D. H. Werner, and T. S. Mayer, *Scientific Reports* **3**, 1 (2013).
- [22] G. Q. Luo, W. Hong, Q. H. Lai, K. Wu, and L. L. Sun, *IEEE Transactions on Microwave Theory and Techniques* **55**, 2481 (2007).
- [23] B. Li and Z. Shen, *IEEE Transactions on Antennas and Propagation* **61**, 3053 (2013).
- [24] Q. Lv, C. Jin, B. Zhang, and R. Mittra, *IEEE Access* **7**, 55833 (2019).
- [25] R.-X. Liao, S.-W. Wong, Y. Li, J.-Y. Lin, B.-Y. Liu, F.-C. Chen, and Z. Quan, *IEEE Access* **8**, 113675 (2020).
- [26] K. Sarabandi and N. Behdad, *IEEE Transactions on Antennas and Propagation* **55**, 1239 (2007).
- [27] F. Bayatpur and K. Sarabandi, *IEEE Transactions on Microwave Theory and Techniques* **56**, 774 (2008).
- [28] O. Luukkonen, C. Simovski, G. Granet, G. Goussetis, D. Lioubtchenko, A. V. Raisanen, and S. A. Tretyakov, *IEEE Transactions on Antennas and Propagation* **56**, 1624 (2008).
- [29] F. Bayatpur, *Metamaterial-Inspired Frequency-Selective Surfaces.*, Ph.D. thesis (2009).
- [30] F. Mesa, R. Rodriguez-Berral, M. Garcia-Vigueras, F. Medina, and J. R. Mosig, *IEEE Transactions on Antennas and Propagation* **64**, 1106 (2015).
- [31] C. Molero, R. Rodriguez-Berral, F. Mesa, and F. Medina, *Physical Review E* **95**, 023303 (2017).
- [32] H. A. Haus, *Waves and Fields in Optoelectronics* (Prentice-Hall, 1984).
- [33] S. Fan and J. D. Joannopoulos, *Physical Review B* **65**,

- 235112 (2002).
- [34] W. Suh, Z. Wang, and S. Fan, *IEEE Journal of Quantum Electronics* **40**, 1511 (2004).
- [35] L. Maloratsky, *Passive RF and Microwave Integrated Circuits* (Elsevier, 2003).
- [36] F. Alpegiani, N. Parappurath, E. Verhagen, and L. Kuipers, *Physical Review X* **7**, 021035 (2017).
- [37] H. Zhang and O. D. Miller, arXiv preprint arXiv:2010.08650 (2020).
- [38] Q. Li, T. Wang, Y. Su, M. Yan, and M. Qiu, *Optics Express* **18**, 8367 (2010).
- [39] C. W. Hsu, B. G. DeLacy, S. G. Johnson, J. D. Joannopoulos, and M. Soljacic, *Nano Letters* **14**, 2783 (2014).
- [40] E. Ching, P. Leung, A. M. van den Brink, W. Suen, S. Tong, and K. Young, *Reviews of Modern Physics* **70**, 1545 (1998).
- [41] P. Lalanne, W. Yan, K. Vynck, C. Sauvan, and J.-P. Hugonin, *Laser & Photonics Reviews* **12**, 1700113 (2018).
- [42] W. Yan, R. Faggiani, and P. Lalanne, *Physical Review B* **97**, 205422 (2018).
- [43] P. T. Kristensen, R.-C. Ge, and S. Hughes, *Physical Review A* **92**, 053810 (2015).
- [44] J. S. Jensen and O. Sigmund, *Laser & Photonics Reviews* **5**, 308 (2011).
- [45] N. Aage and V. Egede Johansen, *International Journal for Numerical Methods in Engineering* **112**, 283 (2017).
- [46] M. A. Popović, C. Manolatu, and M. R. Watts, *Optics Express* **14**, 1208 (2006).
- [47] See Supplemental Material.
- [48] W. L. Brogan, *Modern Control Theory* (Pearson education India, 1991).
- [49] The optimization can for example be done using an augmented Lagrangian method [75]. Gradients can also be effectively computed using automatic differentiation [76] or even analytically, when  $\Lambda = I$ .
- [50] J. D. Joannopoulos, S. G. Johnson, J. N. Winn, and R. D. Meade, *Photonic Crystals: Molding the Flow of Light*, 2nd ed. (Princeton University Press, 2008).
- [51] Comsol Multiphysics<sup>®</sup> v5.1, www.comsol.com, COMSOL AB, Stockholm, Sweden.
- [52] T. Tischler and W. Heinrich, *IEEE Transactions on Microwave Theory and Techniques* **48**, 2249 (2000).
- [53] B. Kettner, *Detection of spurious modes in resonance mode computations: Pole condition method*, Ph.D. thesis, Free University Berlin (2012).
- [54] L. Nannen and M. Wess, ASC Report, TU Wien **15** (2016).
- [55] A. Taflove and S. C. Hagness, *Computational Electrodynamics: The Finite-difference Time-Domain method* (Artech house, 2005).
- [56] P. Bienstman, “CAMFR: CAvity Modeling FRamework,” <http://camfr.sf.net>.
- [57] K. B. Dossou, L. C. Botten, A. A. Asatryan, B. C. P. Sturmberg, M. A. Byrne, C. G. Poulton, R. C. McPhedran, and C. M. de Sterke, *J. Opt. Soc. Am. A* **29**, 817 (2012).
- [58] T. Paul, C. Menzel, W. Śmigaj, C. Rockstuhl, P. Lalanne, and F. Lederer, *Phys. Rev. B* **84**, 115142 (2011).
- [59] A. E. Miroshnichenko, S. Flach, and Y. S. Kivshar, *Reviews of Modern Physics* **82**, 2257 (2010).
- [60] One could, for example, use the approximation that, within the bandwidth of each high- $Q$  resonance in Eq. (15),  $C(\omega) \approx C(\omega_n)$ , which translates to substituting  $C_{pq} \rightarrow C_{pq,n}$  in the symmetrization condition Eq. (16). However, this only gives an approximate condition that does not improve much on the original result.
- [61] This should not be confused with a symmetric  $S$  matrix, which holds for a *reciprocal* system.
- [62] L. Maleki, A. Matsko, A. Savchenkov, and V. Ilchenko, *Optics Letters* **29**, 626 (2004).
- [63] In other words, it is not possible to obtain high- $Q$  modes verifying Eq. (19) with complex  $\gamma$  without additional modes proximal enough to form a frequency-dependent  $C$ .
- [64] É. Chéron, S. Félix, and V. Pagneux, *Physical Review Letters* **122**, 125501 (2019).
- [65] M. A. Al-Joumayly and N. Behdad, *IEEE Transactions on Antennas and Propagation* **59**, 4542 (2011).
- [66] M. Li, M. A. Al-Joumayly, and N. Behdad, *IEEE transactions on antennas and propagation* **61**, 1166 (2012).
- [67] S. B. Glybovski, S. A. Tretyakov, P. A. Belov, Y. S. Kivshar, and C. R. Simovski, *Physics Reports* **634**, 1 (2016).
- [68] A. Ahmed, I. A. Goldthorpe, and A. K. Khandani, *Appl. Phys. Rev.* **2**, 011302 (2015).
- [69] O. Tsilipakos, T. Koschny, and C. M. Soukoulis, *ACS Photonics* **5**, 1101 (2018).
- [70] W. T. Chen, A. Y. Zhu, and F. Capasso, *Nat. Rev. Mat.* **5**, 604 (2020).
- [71] H. M. Nussenzveig, *Causality and Dispersion Relations* (Academic Press, 1972).
- [72] A. I. Markushevich, *Theory of Functions of a Complex Variable* (American Mathematical Soc., 2013).
- [73] W. R. Sweeney, C. W. Hsu, and A. D. Stone, *Physical Review A* **102**, 063511 (2020).
- [74] J. T. Conway, *IEEE Transactions on Magnetics* **43**, 1023 (2007).
- [75] A. R. Conn, N. I. Gould, and P. Toint, *SIAM Journal on Numerical Analysis* **28**, 545 (1991).
- [76] J. Revels, M. Lubin, and T. Papamarkou, arXiv:1607.07892 [cs.MS] (2016).
- [77] S. G. Johnson, “Notes on perfectly matched layers (PMLs),” <https://math.mit.edu/~stevenj/18.369/pm1.pdf> (2010).

## Supplemental Material

### I. GUIDELINES FOR FINITE-ELEMENT CALCULATION OF EIGENMODES FOR USE IN QNMT

Our QNMT and filter-design method rely on the calculation of the system resonances, including low- $Q$  modes, which may be spread across the complex- $\omega$  plane and may include a mode with zero real frequency ( $\omega_n = 0 - i\Gamma_n$ )—often required for bandstop filters and arising from disconnected metallic components. Accurate numerical solution of the Maxwell equations for such eigen-modes can be challenging due to issues arising from spatial discretization, truncation of the simulation domain in open systems, and “spurious modes” that do not correspond to physical resonance modes [52–54]. These can “pollute” the complex- $\omega$  plane and thus make it difficult to find the system’s low- $Q$  modes. For subwavelength metallic structures like those considered here, where quasi-static resonances can be sensitive to small spatial features, finite-element methods are attractive because they enable nonuniform meshing. In our finite-element calculations of eigenmodes (using COMSOL Multiphysics [51]), we observed some simulation-parameter choices that seem to improve the QNM calculations:

- Our QNMT is mostly applicable to CPMs with a frequency-independent transverse field profile. Thus, while computing QNMs, a “scattering boundary condition” (SBC) matching each CPM’s profile should always be used at its open boundary [even at the end of a “perfectly matched layer” (PML)], as it greatly improves convergence.

- In the cladding (and in the PML when present), to minimize spurious reflections from changes in discretization one should use a mesh that is periodic (or nearly so) in the direction orthogonal to the boundary (where scattered waves should escape) [55, 77]. In COMSOL, we employed a “swept” mesh for this reason, and found it to give smoother convergence of the complex eigenfrequencies with mesh density compared to a standard tetrahedral mesh and to work better for modes with zero real frequency.

- The density of spurious modes worsens as the computational domain (the cladding) around the scatterer increases and in the presence of a PML surrounding the cladding. Therefore, at least initially, during the process of identifying the spectrum of system QNMs (especially the low- $Q$  ones), it is advisable to use a very small cladding without a PML, thus only with the SBC placed close to the scatterer, to push the spurious modes deeper into the complex- $\omega$  plane. This setup should clear them, up to the first branch point (e.g. diffraction or cutoff frequency). Moreover, for a zero-frequency mode, a PML is incapable of properly absorbing the exponential increase of its field, so this setup with only a SBC is necessary.

- Even if the spurious modes have been pushed away, locating the low- $Q$  (and zero-frequency) QNMs initially may require searching for a large number of them and good initial complex-frequency guesses. In some convenient cases, the initial guesses can be provided by the analytically-solveable modes of an effective average structure. For our microwave metasurface examples, when large metal surfaces are used [e.g. in Fig. 6(b)], one can consider the average refractive index in the two regions outside the outermost of these metal surfaces (to the left of the first and to the right of the last) to create for each a uniform metal-backed dielectric slab. The modes of these two slabs with  $\sigma \approx (0, \infty)$  [equivalent to  $\sigma = (1, -1)$  for symmetric structures] can be calculated analytically. On the contrary, when there is little metal [e.g. in Figs. 2, 6(c)], the average refractive index of the entire structure forms an effective dielectric slab with same total thickness, whose modes are the equally-spaced, alternating even/odd resonances of a Fabry–Perot cavity [41], including the one at zero frequency (see Appendix D). In all cases, these analytical complex-frequency values  $\omega_n^g$  can provide good initial guesses for the system low- $Q$  QNMs.

- Regarding how many modes one needs in QNMT to calculate the background response  $C$  accurately enough, one observation is that a (low- $Q$ ) mode  $\omega_n = \Omega_n - i\Gamma_n$  will have an effect at real frequency  $\omega$ , if  $\omega$  lies within a bandwidth proportional to the resonance linewidth, namely if  $|\omega - \Omega_n|/\Gamma_n <$  some number, which depends on the level of accuracy required (e.g.  $-50$  dB stopband transmission will require a very low error tolerance). Obviously, when a mode has very large  $\Gamma_n$ , it can play a role even if it is very distant and it may be very difficult to locate. In those cases [e.g. in Fig. 6(c)], it may be easier to estimate  $C = \bar{S}^{-1}S$ , with  $S$  from a direct simulation and  $\bar{S}$  from a QNMT estimate using only the high- $Q$  modes.

- Finally, after the first step of identifying all relevant QNMs, a larger cladding and/or a PML can be used to respectively allow the QNM near field to decay and/or be absorbed and thus to obtain a more precise computation of its  $\omega_n$  and  $D_{pn}$  (especially for high- $Q$  modes) for use in QNMT or filter design. During optimization, such a setup, with an initial guess given by the filter center frequency  $\omega_c$  and a large number of searched modes may be good enough to precisely calculate all needed QNMs. If it fails for low- $Q$  ones, a separate calculation with initial guess  $\omega_c - i\text{Im}(\omega_n^g)$  (and perhaps the original SBC-only setup) might provide those.

## II. CHOICE OF BOUNDARY FOR $D$ CALCULATION

In our QNMT formulation, we suggest to calculate the coupling coefficient  $D_{pn}$  as an overlap between the QNM  $n$  and the CPM  $p$  at the latter's cross-section  $c'_p$ , which first touches the scatterer boundary. A reasonable question is whether such a choice is always appropriate, especially in unusual geometries where a thin “needle” sticks out from the scatterer or when very-low-index materials surround the scatterer. In such scenarios, the QNMs are expected to be localized close to the center of the scatterer and likely are already exponentially increasing inside the suggested outermost boundary. Here, we study a simple such photonic structure to explain the physics that come into play to render our boundary choice indeed suitable.

A plane wave at frequency  $f = \omega/2\pi$  is normally incident on a uniform dielectric slab of relative permittivity  $\epsilon_s = 9$  and thickness  $t$  that is attached to another slab of the same thickness but with  $\epsilon = 1.1$  (Fig. S1 inset). As a reference, the limiting symmetric system with  $\epsilon = 1$  and ports' cross-sections A, B' on the boundaries of the  $\epsilon_s$  slab has the response shown in Fig. S1 for (a) the poles (blue circles) with  $\sigma_n = \pm 1$ , (b) transmission amplitude and (c) phase delay (blue dashed lines). The response of the actual test system (shown with black 'x' and lines) obviously approaches that of the limiting case in amplitude and has an additional phase delay due to the propagation through the  $\epsilon$  slab B'–B [Fig. S1 (b,c)]. It may be tempting to think that the two systems should have the same QNMT parameters ( $\omega_n, \sigma_n$ ). However, its high- $Q$  modes now have  $\sigma_n$  different from  $\pm 1$  (e.g.  $\omega_n t/2\pi c = 0.165 - 0.039i$  has  $\sigma_n = -0.66 - 1.04i$ ), exactly because they are calculated on our suggested boundary  $c'_p = B$  and the structure between A–B is asymmetric. How can we then expect QNMT to give an accurate prediction? The key lies in a set of very-low- $Q$  modes  $\omega_n^C$  that are supported mainly by the weakly scattering  $\epsilon$  slab [Fig. S1(a) below the inset] and have highly asymmetric  $|\sigma_n^C| \gg 1$  (e.g.  $\omega_n^C t/2\pi c = 0.24 - 0.23i$  has  $\sigma_n^C = 344 - 531i$ ). As  $\epsilon \rightarrow 1$ , their  $\Gamma_n^C \rightarrow \infty$  and their contribution to the QNMT prediction of  $S$  is the needed additional phase delay through B'–B.

We conclude that all structural features contribute to scattering, which may be expressed via low- $Q$  modes that need to be included in the QNMT expansion. This justifies our choice of surface for the calculation of  $D$  to be the closest port cross-section that encloses the entire scatterer. However, this may lead to practical issues when very-low- $Q$  modes are difficult to calculate. In those cases, the  $S = \bar{S}C$  formulation may come in handy (see analysis of second-order bandstop elliptic filter).

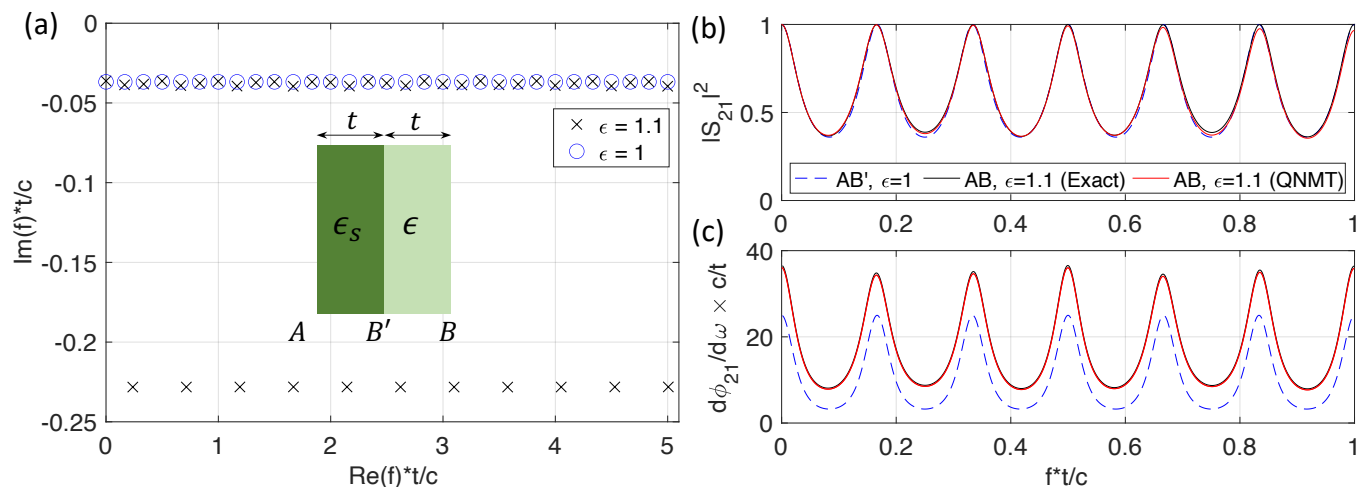


FIG. S1. Normally incident plane wave transmission through dielectric slabs with  $\epsilon_s = 9$ ,  $\epsilon = 1.1$  and thickness  $t$  (black for exact result and red for QNMT prediction), and comparison to the limiting case of  $\epsilon = 1$  (blue for exact result). (a) Geometry and poles, (b) amplitude and (c) group delay: the small shift is due to the extra propagation through the B'–B slab, predicted by QNMT primarily via the contribution of the low- $Q$  modes.

## III. 4-PORT METASURFACE VIA COUPLED POLARIZATIONS EXAMPLE

In Fig. S2, we provide the geometrical details (see caption) and more simulation results for our QNMT modeling of the 4-port microwave metasurface with rotated apertures. The  $S$ -matrix obtained through QNMT Eq. (7) without the correction of Eq. (11) is unitary but not symmetric, as indicated by the large amounts of  $|S_{pq} - S_{qp}| \neq 0$  asymmetry shown in the bottom-left plot. As discussed in the main text, one can see that also the amplitudes are non-symmetric

$|S_{pq}| \neq |S_{qp}|$  for this system with more than two ports (blue lines). These issues are resolved after fine-tuning the  $D$  coefficients [Eq. (11)], resulting in a more accurate and physical *unitary and symmetric*  $S$  matrix (red lines).

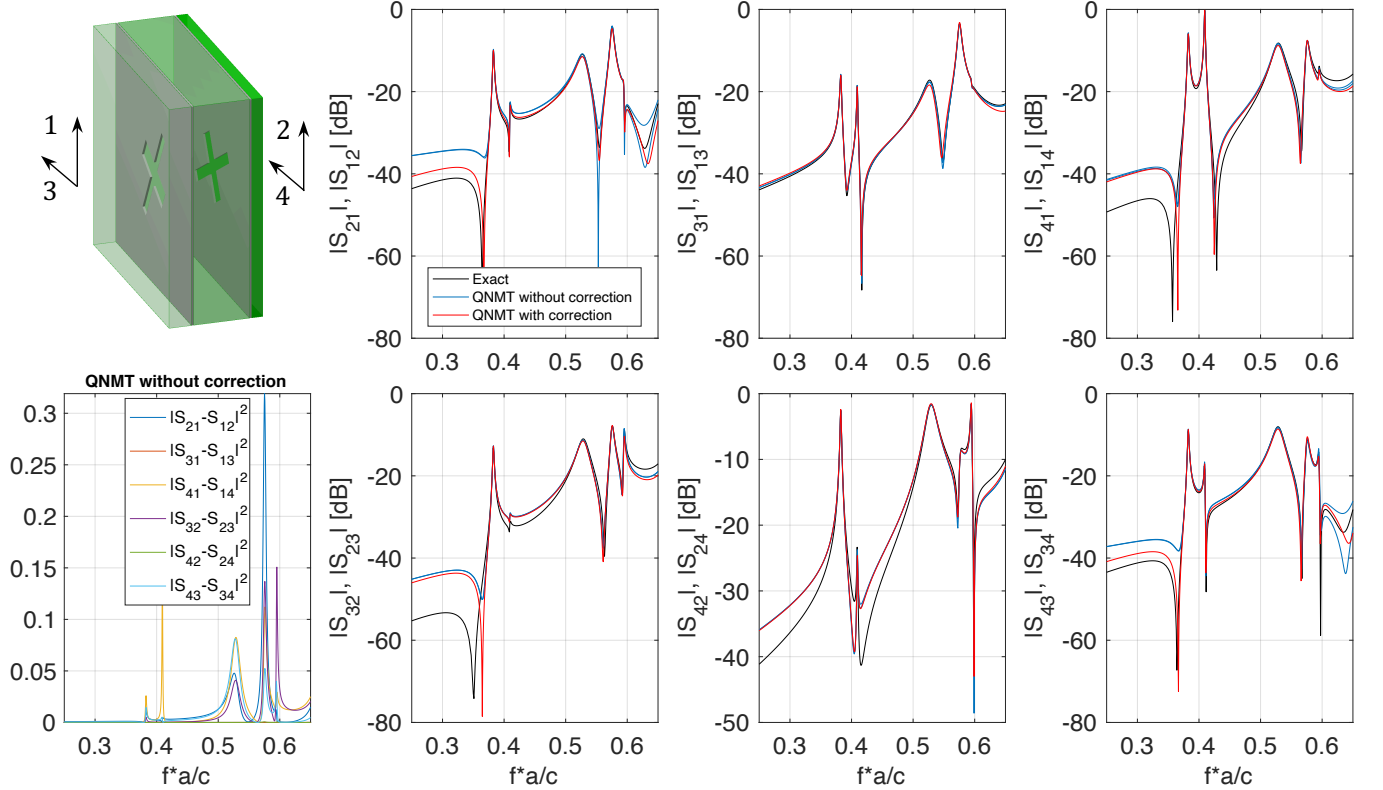


FIG. S2. Example of 4-port structure with ports (1,3) and (2,4) corresponding to the two polarizations on the left (1,2) and right (3,4) sides of the structure. The metasurface is formed by two planar periodically patterned (period  $a = 15\text{mm}$ ) metallic sheets sandwiched between three uniform dielectric layers with  $\epsilon = (2, 3, 5)$  and thicknesses  $t/a = (0.1, 0.05, 0.15)$ . The two metallic sheets are patterned with same cross-like apertures [with widths  $(0.05a, 0.1a)$  and lengths  $(0.5a, 0.3a)$  in two orthogonal directions], which are rotated by angles  $30^\circ$  and  $60^\circ$  with respect to the polarization of port 1.

#### IV. TRANSFER-MATRIX FORMALISM

For a 2-ports system, the (forward) transfer matrix is defined as:

$$\begin{pmatrix} s_{+1} \\ s_{-1} \end{pmatrix} = \begin{pmatrix} T_{11} & T_{12} \\ T_{21} & T_{22} \end{pmatrix} \begin{pmatrix} s_{-2} \\ s_{+2} \end{pmatrix} \quad (\text{S1})$$

and is related to the scattering matrix via the transformation:

$$T = \frac{1}{S_{21}} \begin{pmatrix} 1 & -S_{22} \\ S_{11} & -\det(S) \end{pmatrix}. \quad (\text{S2})$$

In terms of the  $T$  matrix, on the real- $\omega$  axis, realness is expressed as  $T^*(i\omega) = T(-i\omega)$  and energy conservation as  $|T_{11}|^2 - |T_{21}|^2 = |T_{22}|^2 - |T_{12}|^2 = 1$ ,  $T_{11}^*T_{12} = T_{21}^*T_{22}$ , while reciprocity holds anywhere on the complex- $\omega$  plane and is written as  $\det(T) = 1$ .

At a system complex pole  $\omega_n$ , there are non-zero outgoing fields ( $s_{-1}, s_{-2} \neq 0$ ) without an input ( $s_{+1} = s_{+2} = 0$ ), so  $T_{11}(\omega_n) = 0$ . Since then  $D_{1n} \propto s_{-1}$  and  $D_{2n} \propto s_{-2}$ , the ports-coupling ratio of the mode is  $\sigma_n = 1/T_{21}(\omega_n)$  and reciprocity further mandates  $T_{12}(\omega_n) = -1/T_{21}(\omega_n) = -\sigma_n$ .

The types of filters we are interested in satisfy  $S_{22} = \gamma S_{11}$ , namely  $T_{12} = -\gamma T_{21}$ . Therefore, for reciprocal such filters, we get  $\sigma_n^2 = -T_{12}(\omega_n)/T_{21}(\omega_n) = \gamma$ , as in Eq. (19) of the main text. (Reminder that, if realness must hold, then  $\gamma = \pm 1$ .)

Inversely, consider a unitary reciprocal system where all the modes verify  $\sigma_n^2 = \gamma$ . We write  $S_{pq}(\omega) = A_{pq}(\omega)/P(\omega)$ , where  $P(\omega) = \prod_n (\omega - \omega_n)$  includes all the  $2N$  poles  $\omega_n$  and  $A_{pq}(\omega)$  is a polynomial of degree at most  $2N$ , so Eq. (S2) implies that  $T_{12}(\omega) = -A_{22}(\omega)/A_{21}(\omega)$  and  $T_{21}(\omega) = A_{11}(\omega)/A_{21}(\omega)$ . At a pole, we have  $T_{12}(\omega_n) = -\sigma_n^2 T_{21}(\omega_n) = -\gamma T_{21}(\omega_n)$ , thus  $A_{22}(\omega_n) - \gamma A_{11}(\omega_n) = 0$  [because  $A_{21}(\omega_n) \neq 0$ ]. Since the degree of  $A_{22} - \gamma A_{11}$  is at most  $2N$ , we then have  $A_{22}(\omega) - \gamma A_{11}(\omega) = \alpha P(\omega) \Leftrightarrow S_{22} = \gamma S_{11} + \alpha$ , where  $\alpha$  is a constant. Now, assuming a unitary system, we have  $|S_{22}|^2 = |\gamma S_{11} + \alpha|^2 = |S_{11}|^2 \Leftrightarrow |\alpha|^2 + 2\text{Re}[\alpha^* \gamma S_{11}(\omega)] = 0$  at *all* real frequencies  $\omega$ , leading to  $\alpha = 0$  and thus  $S_{22} = \gamma S_{11}$ .

## V. QNM PARAMETERS FOR STRUCTURES

Here, we provide all the QNMs computed via finite-element simulations. The computed QNM-to-CPM ratios are indicated by  $\sigma^c$ , while the ones fine-tuned by Eq. (11) of the main text are denoted by  $\sigma$ . The modes used to calculate the background  $C$  matrix are marked in bold. For simplicity,  $\Omega$  and  $\Gamma$  in the tables denote the dimensionless frequency values as defined in the corresponding figures.

- Normal incidence on microwave metasurface of Fig. 2:

$\Omega$	<b>0</b>	0.2020	0.2929	<b>0.3510</b>	<b>0.5099</b>	0.6207	0.6431	0.6539	0.6932	0.7395
$\Gamma$	<b>0.0699</b>	0.0136	0.0218	<b>0.0625</b>	<b>0.0905</b>	0.0029	0.0145	0.0048	0.0048	0.0363
$\sigma^c$	<b>0.98</b>	-1.01+0.09i	0.14+0.01i	<b>1.23+4.29i</b>	<b>-0.27+0.11i</b>	-0.81+0.18i	-0.07+0.19i	-0.26-1.70i	-0.93-0.36i	0.89+0.2i
$\sigma$	<b>1.00</b>	-1.04+0.07i	0.14+0.02i	<b>1.14+4.50i</b>	<b>-0.28+0.09i</b>	-0.78+0.12i	-0.09+0.20i	-0.05-1.67i	-0.94-0.61i	0.75+0.3i
$\Gamma_{\text{nr}}$	<b>0</b>	0.0011	0.0016	<b>0.0016</b>	<b>0.0021</b>	0.0027	0.0026	0.0029	0.0033	0.0034

- 4-port metasurface via coupled polarizations of Fig. 3(a):

$\Omega_n$	0.3826	0.4093	0.5288	0.5753	0.5948	0.6753
$\Gamma_n$	0.0011	0.0007	0.0095	0.0029	0.0011	0.0064
$\sigma_{1,2n}^c$	-1.44-0.36i	-0.07+0.01i	2.00+0.62i	0.57+0.23i	-17.60-5.09i	1.68+1.69i
$\sigma_{1,2n}$	-1.50-0.13i	-0.06+0.03i	2.24-0.21i	0.59-0.06i	-14.57+3.13i	3.17-0.01i
$\sigma_{1,3n}^c$	0.71+0.00i	0.15+0.03i	1.01-0.02i	0.66-0.03i	-3.62+2.09i	-0.71-0.03i
$\sigma_{1,3n}$	0.72+0.00i	0.13+0.03i	1.01-0.03i	0.70-0.02i	-2.40+1.190i	-0.72-0.03i
$\sigma_{1,4n}^c$	-2.32-0.60i	1.20+0.25i	2.83+0.79i	0.43+0.00i	9.97+4.22i	-1.37-1.40i
$\sigma_{1,4n}$	-2.37-0.23i	1.18+0.01i	3.11-0.36i	0.41-0.17i	8.90-1.07i	-2.60+0.00i

- Oblique incidence on 2d photonic metasurface of Fig. 3(b):

$\Omega$	0	0.1869	0.3157	0.362	0.427	0.444	0.499
$\Gamma$	0.0402	0.0377	0.0026	0.0265	0.0012	0.0107	0.0106
$\sigma^c$	0.9533	-0.679+0.03i	0.345+0.274i	0.992-0.051i	1.08-0.181i	-0.841+0.062i	-1.71+1.19i
$\sigma$	0.9728	-0.689-0.019i	0.289+0.329i	1.11+0.088i	1.21+0.032i	-0.787-0.073i	-1.99+0.865i

$\Omega$	0.5219	0.5716	0.6044	0.6514	0.6737	0.7231
$\Gamma$	0.0122	0.00024	0.0011	0.016	0.0065	0.0052
$\sigma^c$	-0.078+0.24i	-0.051+0.137i	-3.09-0.498i	0.409+0.012i	1.39+3.76i	0.246-0.008i
$\sigma$	-0.125+0.221i	-0.081+0.120i	-2.96-1.43i	0.369+0.155i	0.769+5.40i	0.266-0.024i

In the case of filter design, we remind that good approximate solutions with complex  $\gamma = e^{i\varphi}$  can be found, so we allow a common phase  $\sqrt{\gamma}$  for the ratios  $\sigma$  during optimization. Deviations of the final computed  $\sigma^c/\sqrt{\gamma}$  from the ideal  $\pm 1$  or  $\pm i$  shown below lead to only small errors in the ISF designs. For symmetric structures, all computed  $\sigma^c$  are equal to  $\pm 1$  anyway. (Note that, after the design optimization process is completed, we do not care to fine-tune  $\sigma$  for QNMT modeling, since in Figs. 5,6 we only show the exact transmission spectra from direct frequency-domain simulations anyway.)

- Third-order bandpass filters of Fig. 6:

Type	Butterworth ( $\varphi = 0$ )			Chebyshev ( $\varphi = 0$ )			Inverse Chebyshev ( $\varphi = -0.07\pi$ )		
$\Omega$	0.9774	1.0010	1.0210	0.9788	1.0009	1.0223	0.9728	0.9975	1.0254
$\Gamma$	0.0127	0.0251	0.0123	0.0079	0.0154	0.0075	0.0119	0.0341	0.0128
$\sigma^c/\sqrt{\gamma}$	1	-1	1	1	-1	1	-0.94+0.00i	1.05+0.02i	-0.98+0.03i

Type	Elliptic 2% ( $\varphi = -0.066\pi$ )			Elliptic 6% ( $\varphi = -0.059\pi$ )			Elliptic 10% ( $\varphi = -0.075\pi$ )		
$\Omega$	0.9885	0.9995	1.0101	0.9718	0.9987	1.0274	0.9516	0.9972	1.0504
$\Gamma$	0.0032	0.0086	0.0028	0.0076	0.0218	0.0078	0.0124	0.0392	0.0145
$\sigma^c/\sqrt{\gamma}$	-1.04-0.14i	1.16+0.03i	-1.10+0.17i	-1.04+0.03i	0.91-0.01i	-1.01-0.04i	-1.04-0.15i	1.19+0.00i	-1.03+0.15i

- Third-order bandstop filter of Fig. 7(a): ( $\varphi = -0.16\pi$ )

$\Omega$	0.949	1.004	1.065
$\Gamma$	0.0156	0.0809	0.0158
$\sigma^c/\sqrt{\gamma}$	0.95+0.04i	-0.97+0.00i	0.97-0.04i

- Second-order bandpass filter of Fig. 7(b):

$\Omega$	<b>0.738</b>	<b>0.751</b>	0.996	1.004	<b>1.186</b>	<b>1.191</b>	<b>1.289</b>	<b>1.362</b>
$\Gamma$	<b>0.297</b>	<b>0.301</b>	0.0031	0.0031	<b>0.0012</b>	<b>0.011</b>	<b>0.0084</b>	<b>0.0007</b>
$\sigma^c$	<b>1</b>	<b>-1</b>	-1	1	<b>-1</b>	<b>1</b>	<b>-1</b>	<b>1</b>

The modes marked in bold lead to  $|C_{21}(\omega_c)| = -24.9$  dB and  $\beta = C_{11}C_{21}^*/|C_{11}C_{21}| = -i$ .

- Second-order bandstop filter of Fig. 7(c):

$\Omega$	<b>0</b>	0.954	1.042	<b>1.109</b>	<b>1.459</b>	<b>1.481</b>	<b>1.892</b>
$\Gamma$	<b>0.851</b>	0.0313	0.0343	<b>0.993</b>	<b>0.0156</b>	<b>0.0024</b>	<b>0.945</b>
$\sigma^c$	<b>1</b>	-1	1	<b>-1</b>	<b>1</b>	<b>-1</b>	<b>1</b>

Note that the ‘‘Fabry-Perot’’ modes here have such a large  $\Gamma$  that higher-order such modes will still have an effect at frequencies around  $\omega \sim \omega_c$ . However, they lie deep inside the diffraction zone, so they are hard to identify from spurious modes. Therefore, as explained in the main text, we calculated more accurately  $C(\omega_c) = \bar{S}^{-1}(\omega_c)S(\omega_c)$ , with  $\bar{S}$  and  $S$  obtained at  $\omega_c$  from QNMT on the two high- $Q$  modes and a direct computation respectively. The optimized result is then indeed  $|C_{21}(\omega_c)| = -0.25$  dB and  $\beta = i$ .